NONINVASIVE PREDICTION OF FAILURE IN TRABECULAR BONE WITH SIMULATED REGULARLY SHAPED LYTIC DEFECTS

by

James Hong

B.S. Mechanical Engineering - Purdue University, 1994

SUBMITTED TO THE DEPARTMENT OF MECHANICAL ENGINEERING
IN PARTIAL FULFILLMENT OF THE REQUIREMENTS FOR THE DEGREE OF

MASTER OF SCIENCE IN MECHANICAL ENGINEERING
AT THE
MASSACHUSETTS INSTITUTE OF TECHNOLOGY

June 1997

Signature of Author .....
Department of Mechanical Engineering
February 1997

Certified by .....
John A. Hipp
Director, Institute for Spinal Disorders, Baylor College of Medicine, Houston TX
Thesis Supervisor

Certified by .....
Brian D. Snyder
Orthopedic Surgeon, Children's Hospital, Boston MA
Thesis Supervisor

Certified by .....
Wilson C. Hayes
Director, Orthopedic Biomechanics Laboratory, Beth Israel Hospital
Thesis Reader

Accepted by .....
Ain A. Sonin
Professor of Mechanical Engineering
Chairman, Committee on Graduate Students

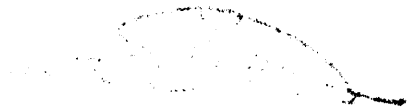

NONINVASIVE PREDICTION OF FAILURE IN TRABECULAR BONE WITH SIMULATED REGULARLY SHAPED LYTIC DEFECTS

by

James Hong

Submitted to the Department of Mechanical Engineering
on February 17, 1997 in partial fulfillment of the
requirements for the Degree of Master of Science in
Mechanical Engineering

ABSTRACT

Pathologic fracture is a common problem in patients who suffer from metastatic or benign disease of the skeletal system. In the United States an astonishing 1.2million individuals are diagnosed with cancer each year, and 60-80% of primaries will metastasize to bone. It is common for asymptomatic children to harbor benign tumors; 33% to 50% of children will be diagnosed with benign tumors incidentally. Fortunate children will not experience physical trauma, and the tumors will become substituted with normal bone cells, however, others will suffer fracture under loads experienced during typical activities. The quandary in clinical orthopedics is the subjective method used to prescribe treatment for pathologic bone. Orthopedic surgeons rely on interpretation of *qualitative* images from plane radiograph and CT scans to understand the nature of the defect and its effect on the structural capacity of bone. These methods have never been proven to be either sensitive or specific.

This research is part of an effort to develop noninvasive means to predict the failure of pathologic bone. To establish optimal imaging techniques and the effect of defects in trabecular bone, we investigated the ability of magnetic resonance imaging (MRI), dual energy *x*-ray absorptiometry (DXA), and quantitative computed tomography (QCT) to predict the failure of trabecular bone with simulated defects.

Trabecular bone harvested from thoracic to lumbar whale vertebral bodies was found to have mechanical properties that are related to density but that are different from human trabecular bone. The elastic and shear modulus exhibited a power law and linear relationship to bone density respectively ($E=3901\rho_{app}^{1.67}$, $r^2=0.955$; $G=745.4\rho_{ash}-101$, $r^2=0.930$ ~ $p<0.001$). The ash density of the specimens used in this study ranged between 0.1g/cc to 1.1g/cc, and the tissue density and bone mineral content across the three whale species did not vary more than 5%.

Using a proton density sequence, a porosity phantom, and constant tissue properties, we found that *in-vivo* MRI measurements of density and cross-sectional geometry correlated with QCT measurements (Density: $r^2=0.923$; Max. Moment of Inertia: $r^2=0.971$ ~ $n=14$, $p<0.01$).

Based on beam theory and the assumption that trabecular bone can be represented as a structure, and that it fails at constant strain, a model was developed to show the proportional relationship between yield load and structural rigidity (GJ, EI, and EA). Cylindrical trabecular specimens with symmetric circular and elongated defects were tested in pure torsion, four-point bending, and uniaxial tension. A strong positive relationship was discovered between failure load in each testing mode and MRI, DXA, and QCT measurements of structural rigidity (MRI: torsion - $r^2=0.852$, bending - $r^2=0.856$, tension - $r^2=0.916$; DXA: $r^2=0.916$, $r^2=0.841$, $r^2=0.926$; QCT: $r^2=0.914$, $r^2=0.909$, $r^2=0.951$ ~ $p<0.001$).

Thesis Supervisors: John A. Hipp - Director of the Institute for Spinal Disorders; Houston, TX
Brian D. Snyder - Orthopedic Surgeon at Children's Hospital; Boston, MA

ACKNOWLEDGEMENTS

Accomplishments in my modest life could not have occurred without the influence and patient participation of many gracious individuals. I am privileged to have known each one of them, and I am grateful for how they have collectively affected my life.

I am humbly grateful for the training I received from my graduate research advisor's Dr. John A. Hipp and Dr. Brian D. Snyder. Although the road was long, no obstacle was too overbearing. John always kept his door open for discussions over career choices and frustrations related to experiments. His analytic prowess and no-nonsense approach many times cleared cloudy thoughts. I have learned much from his honest and benevolent nature. Brian's optimism and ample ideas provided the support and vision necessary to maintain my focus and keep proper perspective on the value of my work.

The orthopedic biomechanics laboratory under the directorship of Wilson C. Hayes is truly a well equipped and staffed organization. Many cohorts at the lab made the stress manageable and long days seem short. In particular, John Tedrow for our talks, Greg Cabe for collaborating on experimental work, and Diane Allen for her encouraging words when the weight of the world seemed heavy on my shoulders.

Professor Normand M. Laurendeau, professor of mechanical engineering at Purdue University, mentioned in passing three characteristics to the success in any endeavor: inspiration, motivation, and perspiration. Throughout my academic career, inspiration in many respects was sown by my undergraduate research advisor, Dr. Leslie A. Geddes and friend, Stanley Reed. Dr. Geddes epitomized devotion for one's professional career, and the significance and fulfillment that can derive from contributing to one's chosen field. His mastery and display of skills taught me the art and humanity associated with engineering; without an open mind, solutions and answers stay well hidden. People are the primary asset to the success of an institution, and should be held with regard before all other aspects. Stan posed questions that stimulated reflection about my goals, or

simply the motivation for waking in the morning. It is simple to become caught up in the requirements of standardized life pursuits, never realizing the purpose, worth, and pleasure behind the efforts. His firm morals and passion for living prove exception to the blind journey commonly observed. Through the latter years of my study, I met an unpretentious and adventure seeking person - Alexandra shined new perspective on myself and challenged me to practice and achieve my ideals, she has brought fresh experience into my routine life.

My fundamental nature was instilled by my family, to whom I honor and thank for their steadfast devotion to my well-being. I have never been acquainted with an individual with more perseverance and tolerance for hardship than my mother. Her struggles in this foreign country, has made this place a home and ambitions attainable for her sons. I dedicate this thesis to her. My Uncle's austere influence taught me discipline, and to question my intentions and its affect on others. Selflessness and care from my brother, George, have provided a constant source of encouragement through my trials and triumphs. Regardless of his activities he listened with intent and offered thoughtful advice. And to my Grandmother, I thank for her commitment, and bond she creates between our family's generations.

TABLE OF CONTENTS

CHAPTER 1
INTRODUCTION

1.1 BACKGROUND

Pathologic fractures of the skeletal system are commonly associated with various types of benign and metastatic tumors and metabolic bone diseases. Benign tumors such as fibroxanthoma, fibrous dysplasia, and unicameral bone cysts all exhibit interstitial bone loss, that would decrease the structural capacity. Depending on the severity and load bearing level, pathologic fracture may occur, resulting in intractable pain, loss of function, and morbidity. Thirty-three to 50% of asymptomatic children are diagnosed with benign bone lesions incidentally [1], and are at a risk for fracture under loads experienced during typical activities.

Metastatic bone tumors occur frequently in patients with breast, lung, kidney, thyroid, or prostate cancer [2]. In the United States 1.2 million new cases of cancer are reported each year [3], and 60% to 80% of primaries metastasize to bone [4]. In many of these cases, the patient experiences excruciating pain, and pathologic fracture can result from severe bone loss. Primary bone malignancies are often treated with neoadjuvant chemotherapy prior to surgery; if fracture occurs during this time period, the patient may suffer amputation. It is critical to be aware of the risk for fracture to prevent trauma and associated costs.

Current clinical guidelines for predicting pathologic fracture in adult and children with benign or malignant tumors are inadequate and have never been proven to be sensitive nor specific. Orthopedic surgeons rely primarily on interpretation of *qualitative* images from plane radiographs, computed tomography, and magnetic resonance images to assess strength reduction based on defect size alone. This form of practice provides no objective means of estimating the fracture risk, and may be highly dependent on experience. In one investigation, three orthopedic oncology surgeons were provided radiographs and CT scans of proximal femora with simulated metastatic defects and intact contralateral femurs [5]. Each surgeon was asked to evaluate the relative strength

reductions; there was no consistency between estimations by the physicians nor correlations between experimentally strength reductions and physician estimated strength reductions.

To develop non-invasive, cost-effective methods for predicting fracture risk in patients with pathologic bone defect, we first investigated optimal imaging techniques to predict failure in trabecular bone with simulated lytic defects. Noninvasive measurements would facilitate treatment planning and resource utilization, and provide guidelines for selecting among various treatment options based on a quantitative assessment of fracture risk.

1.2 Specific Aims and Techniques

1.2.1 Aim 1 - Validation of Whale Trabecular Bone • Only small specimens of standard trabecular bone can be harvested from bovine and porcine sources. Errors in measurement are often associated with small specimens that are subjected to heterogeneous stress gradients [6], and microstructural variations. Using large homogenous trabecular specimens that are affected less by individual trabeculae, errors associated with small specimens are reduced. Whale trabecular bone harvested from the vertebral bodies from various whale species was used as a model for human trabecular bone in this study. The first goal was to compare tissue and mechanical properties of whale trabecular bone with published data for human trabecular bone.

Trabecular cores were harvested from thoracic to lumbar vertebral bodies of three whale species and screened for discontinuity in trabecular orientation and density. Bone material properties were determined using standard measurement techniques [7,8], and uniaxial compression and pure torsion tests were conducted to determine the relationship between elastic and shear moduli and bone density.

1.2.2 Aim 2 - Quantitative MRI • Quantitative magnetic resonance techniques have been used to demonstrate associations between relaxation parameters and bone mechanical properties [9], however it is not possible to obtain cross-sectional geometric properties with these

methods. The second objective of this study was to use magnetic resonance imaging's (MRI) ability to detect substances with proton content to estimate the porosity of trabecular bone, and to use this information to determine bone density and cross-sectional geometry.

Whale trabecular specimens was first used to validate the quantitative MR technique of measuring density of a bone cross-section based on porosity. Measurements were compared with standard quantitative methods using computed tomography (QCT). The study was then extended to *in-vivo* experiments. MR exams of the distal tibia were performed on human volunteers, and density and cross-sectional geometry measurements were compared with QCT measurements of the same scan location.

1.2.3 Aim 3 - Noninvasive Measurement of Structural Properties and Prediction of Failure in Trabecular Bone with Simulated Defects • MRI, dual energy *x*-ray absorptiometry (DXA), and QCT all have unique advantages as quantitative tools. Although DXA has been shown to predict precisely the structural properties of bone [10], it has not been shown to predict the failure load of bones with lytic defects. The primary goal of this study was to determine the ability of MRI, DXA, and QCT to predict the failure load of cylindrical trabecular specimens with simulated symmetric defects based on beam theory.

A prediction model for the failure of trabecular bone with and without defects was developed using beam theory, and the assumption that trabecular bone fails as a structure at a common strain. This model was incorporated into an image processing software (Advanced Visual Systems), and used to analyze MRI and CT scans of cylindrical specimens with circular and elongated slot defects. DXA data were analyzed using a similar prediction model based on the bone density profile of a cross-section. Specimens were separated into three groups, and tested in either pure torsion, four-point bending, or uniaxial tension. MRI, DXA, and CT's ability to predict the failure load was analyzed, and the difference in the effects of circular holes versus slots was compared.

CHAPTER 2
VALIDATION OF WHALE VERTEBRAL TRABECULAR BONE AS A MODEL FOR HUMAN TRABECULAR BONE

2.1 INTRODUCTION

Current models for studying trabecular bone encompass a wide range of animals (bovine, porcine, and canine), and are representative of the density range found in human cancellous bone. However it is difficult to harvest sufficiently large homogenous specimens to avoid heterogenous stress gradients due to end effects [6] and microstructural variations. Large homogenous specimens are influenced less by individual trabeculae and thereby reduce errors associated with small specimens and gauge lengths. In this study we investigate the use of whale-vertebral trabecular bone as a model for human trabecular bone by evaluating bone tissue properties and relationships between modulus and bone mineral density. Elastic modulus was correlated with physical measurements of apparent density. Since there is little information on the relationship of mechanically obtained shear modulus of human trabecular bone and density, shear modulus was correlated with ash density measurements made using quantitative computed tomography (QCT).

2.2 MATERIALS AND METHODS

2.2.1 Specimen Preparation • Trabecular cores were harvested from the vertebral bodies of six whales (Table 1).

Table 1 Species of Whale and Location of Vertebral Body Used in the Study

Species	Source	Maturity	Vertebral Body Used
Physeter macrorynchus	National Marine Fisheries Miami, FL	Juvenile	Lumbar, Caudal
Baelena mystecetus	N Slope Borough Dept of Wildlife Mgt Barrow, AS	Adult	Caudal, Thoracic
Koja Breviaceps	National Marine Fisheries Miami, FL	Adult	Thoracic, Lumbar Caudal

A one-half inch diamond tip coring tool was used to extract specimens in the superior to inferior direction. By designating the distal endplate as the orthogonal-zero reference, the longitudinal axis of the specimens was cored in the direction of predominant trabecular growth. Each 12.7mm diameter core was radiographed at 75KV for 11s and visually screened for natural discontinuities (e.g. vascular channels) and trabeculae misalignment. Nine - 5mm, 19 - 13.5mm, and 10 - 73mm long cylindrical cores were extracted for tissue density measurements, uniaxial compression tests, and torsional tests, respectively.

2.2.2 Bone Density Measurements • Soft tissue within pore spaces was removed using a water jet wash and repeated ultrasonic agitation in 20% concentration chlorine baths [7]. Tissue, apparent density, and ash content were calculated using Equations 1-3.

$$\text{Tissue Density} = \frac{\text{wet mass}}{(\text{bouyant force} / \text{gravity} * \rho_{water})} \qquad \textbf{Equation 1}$$

$$\text{Apparent Density} = \frac{\text{wet mass}}{\text{bulk volume}} \qquad \textbf{Equation 2}$$

$$\text{Ash Content} = \frac{\text{ash weight}}{\text{dry weight}} \qquad \textbf{Equation 3}$$

Applying Archimedes principle, tissue density was determined using the buoyant force and the wet weight of the specimen. The buoyant force was determined by removing air from the pores using a vacuum chamber, and measuring the suspended weight of the specimen in water. Specimens were then placed in a centrifuge at 1000rpm for 15 minutes to remove water from the pores, and the wet mass measured using a closed chamber digital balance (OHAUS Analytical Plus, Florham Park NJ). Dry and ash weights were measured after dehydrating the specimens for 120 hours at 75°C (Equatherm, Melrose Park IL) and ashing them for 24 hours at 600°C (Thermolyne, DuBuque IA), respectively.

Specimens for the torsion tests were encased in saline filled tubes, and placed in a vacuum chamber to remove air from the pore spaces. A hydroxyapatite phantom was scanned with the specimens in a high speed helical CT scanner (GE Medical Systems, Milwaukee WI). Three millimeter thick slices were taken with a 0.234 mm per pixel apparent resolution. Ash density measurements were obtained from an algorithm implemented using AVS software (Advanced Visual Systems, Waltham MA) to convert CT images to bone density images using the hydroxyapatite phantoms [8].

2.2.3 Uniaxial Compression Tests • Specimens were thawed at 21°C and subjected to uniaxial compression until ultimate failure using a platen-platen device adapted to a servohydraulic load frame (Instron 1331; Canton, MA). Platen surfaces were polished to reduce end effects. To accommodate stiffer and stronger specimens with apparent bone density greater than 0.4g/cc, a 2000lb load cell was used, otherwise a 500lb load cell was used for less dense specimens. Specimens were tested under a displacement controlled triangular waveform at a frequency of 0.5Hz. The amplitude of the waveform was increased until the peak strain reached approximately 0.6% to ensure preconditioning cycles in a linear region. The mean was then further increased until rupture. The average strain rate was 1.83%/s. Axial load and cross-head platen-platen displacement were recorded using LabTech Notebook (Laboratory Technologies Corporation, Wilmington MA). Compressive stress was calculated from the ratio of the applied load to the nominal cross-sectional area. Strain was determined as the ratio of the cross-head displacement to the nominal length of the specimen. Young's modulus was defined as the slope of the region from the minimum stress to 75% of the ultimate stress. Once tested, apparent density and ash content measurements were made.

2.2.4 Torsion Tests • Angular displacement was measured using an optical system capable of resolving 3μm displacements in three dimensional space. One millimeter square infrared (IR) reflective markers were attached to the specimen with cyanoacrylate, and its position

monitored in three dimensional space with MacReflex (Sweden), a non-contacting displacement measurement system that emits and registers infrared light. The torsion test was performed using a custom built system adapted to a servohydraulic load frame (Interlaken, Eden Prairie MN) designed specifically to reduce parasitic forces and moments generated by out-of-plane warping of anisotropic material and specimen misalignment [Appendix A]. Specimens were fixed at one end with a manual 5-C collet clamp. A steel cable was wrapped around a collet at the free end to produce a force couple. By applying tension to the cable, a pure torque was applied to the specimen. The torsion system was validated using cast acrylic since it has similar stiffness to bone. Precision and accuracy of the system was determined by comparing measured shear modulus of the acrylic cylinder to the shear modulus calculated from manufacturer's value for the elastic modulus and Poisson's ratio. Four acrylic rods were turned down to 9.5mm cylinders with a gauge length of 25.4mm. This geometry was calculated to displace approximately fifteen degrees at the maximum breaking strength of the cables. The precision of one acrylic cylinder tested seven times at a strain rate of 0.1%/s was 2.3%/s, and the accuracy of four acrylic cylinders tested once each at the same strain rate was within 4% of the calculated shear modulus.

Specimens were thawed at 21°C and coated with black ink to reduce IR reflection. Two reflective markers were spaced 25.4mm apart, collinear with the longitudinal axis. A 56.5Nm loadcell was calibrated to 8.81Nm fullscale output, and the torsional load recorded at 12Hz synchronously with three dimensional coordinates using Biopac (Santa Barbara CA). Tests were conducted under linear displacement control, with a single ramp to failure at an average strain rate of 0.1%/s. The shear modulus was determined from the slope of the linear region of the torque versus angular displacement curve multiplied by the ratio of the gauge length to the bulk polar moment of inertia.

2.2.5 Analysis • The average and coefficient of variation were calculated for tissue density and ash content of the 5mm and 13.5mm long specimens. The power law function,

$y=a\rho^b$, has repeatedly been shown to describe the relationship between elastic modulus and density [11,12,13,14,15,16], and it is proven theoretically for open-celled porous structures [17]. Linear ($y=a\rho+c$) and general non-linear ($y=a\rho^b+c$) regression models were also used to correlate elastic modulus versus apparent density for the compressive data. The goodness of the regressions was evaluated using the coefficient of determination and the *p*-value for the regression. Using the linear regression model as a reference, a Fisher's *z*-test was conducted to determine whether there was a statistical difference between the coefficient of correlation of the power law and nonlinear regression models versus the linear regression model. Ford *et al* showed that a linear relationship exists between shear modulus and density for bovine trabecular bone [18]. Only a linear regression model was used for the shear modulus relationship.

2.3 RESULTS

Specimens from the three whale species did not exhibit a large variation in the tissue density nor bone mineral content (Table 2).

Table 2 Tissue Density and Ash Content of Whale Species Compared to Human

Whale Specie	Tissue Density (g/cc)			Ash Content		
	Mean (g/cc)	Stdev (g/cc)	COV (%)	Mean	Stdev	COV (%)
Physeter macrorynchus	2.10	0.017	0.82	0.655	0.031	4.74
Baelena mystecetus	1.86	0.101	5.40	0.702	0.005	0.68
Koja Breviaceps	1.95	0.006	0.31	0.686	0.002	0.26
Combined	1.97	0.115	5.86	0.681	0.026	3.86
Human [19]	1.94			0.399		

The elastic and shear moduli ranged from 303-1814Mpa and 40-788MPa, respectively. The coefficient of determination for the power and nonlinear regression models were both higher than the linear model. A Fisher's *z*-test showed that the coefficient of correlation for the power law function was statistically different from the linear model, but the nonlinear model was not (Table

3). A strong positive linear relationship exists between shear modulus and ash density (Table 3).

Table 3 Power Law, Linear and Non-Linear Regressions of Modulus versus Bone Density

Regression Model	Modulus	Regression					Fisher's z -test
		a	b	c	p -value	r^2	p -value
Power Law ($y=a\ x^{b}$)	$E=f(\rho_{app})$	3901	1.67		< 0.001	0.955	< 0.05
General Nonlinear ($y=a\ x^{b}+c$)	$E=f(\rho_{app})$	4677	2.17	169	< 0.001	0.829	> 0.50
Linear ($y=a\ x+c$)	$E=f(\rho_{app})$	3370		-453	< 0.001	0.813	---
	$G=f(\rho_{ash})$	745.4		-101	< 0.001	0.930	

Figure 1 illustrates the power and linear trend for elastic and shear modulus, respectively.

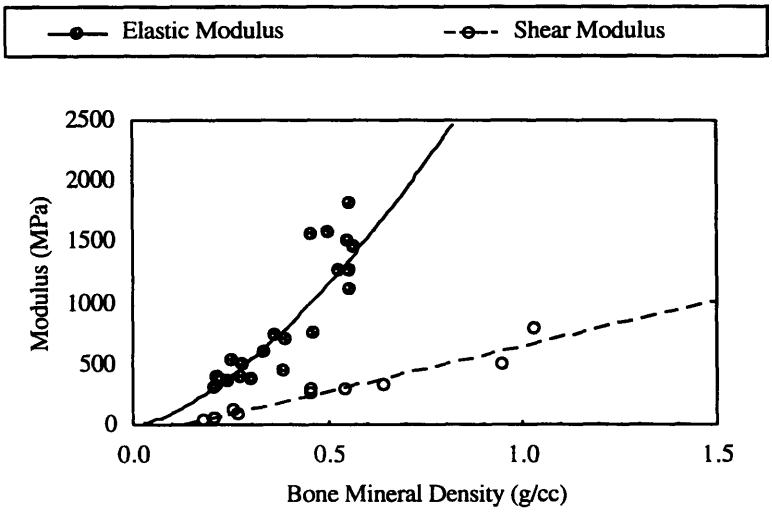

Figure 1 Elastic and Shear Modulus versus Density for Whale Trabecular Bone

2.4 DISCUSSION

Tissue properties of bone from a single specie is normally constant. In this study, specimens were taken from three separate Cetacean species, however, the coefficients of variation for tissue density and ash content were less than 5% for the species grouped together.

The empirical relationship for the elastic modulus in this study is similar in form to reported

relationships in the literature for human trabecular bone (Figure 2).

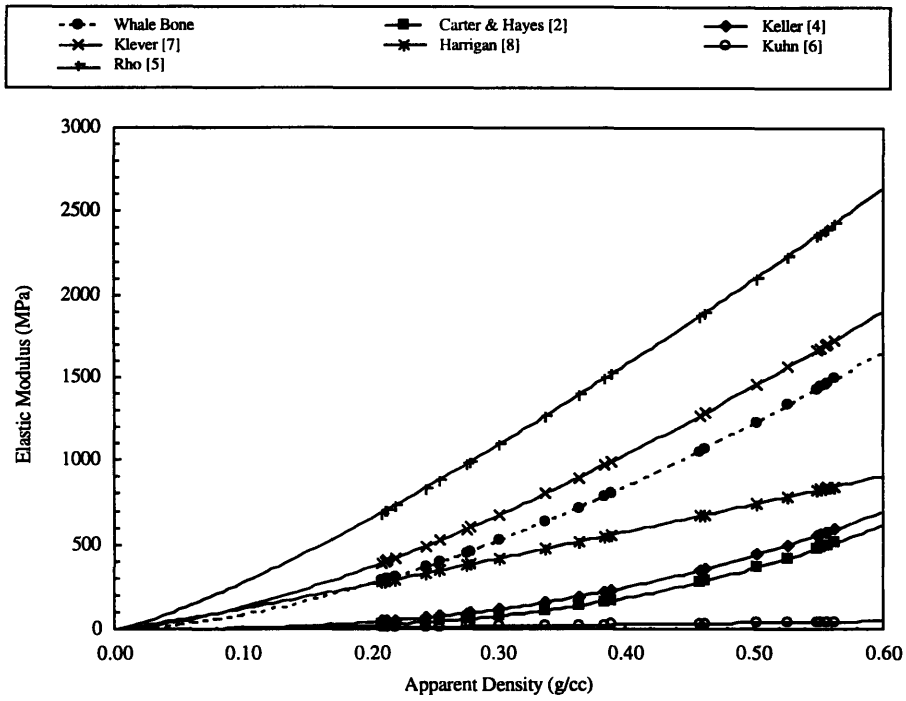

Figure 2 A Comparison between Empirical Relationships of Elastic Modulus versus Apparent Density (Apparent Density of Trabecular Specimens in this Study was Used in the Equations found in the Literature)

Ash content for whale trabecular bone was nearly twice that of human trabecular bone, and it was expected to exhibit a stiffer modulus relationship. The large variation in previously reported relationships between density and modulus for humans is most likely due to inconsistent testing and measurement techniques. Similar to human trabecular bone and open-celled porous structures, the relationship of elastic modulus to density for whale trabecular bone was a power law function, and similar to Ford's *et al* study with bovine trabecular bone, shear modulus was linearly related to bone density.

Due to the limited availability of whale spines, vertebral bodies containing high density trabecular bone ($\rho_{app} > 0.80$ $g/_{cc}$) were not accessible until after tissue property and uniaxial

compression tests were complete.

Based on results in this study, densitometric and mechanical properties of whale trabecular bone do not accurately reflect human bone, however, the relationship between density and modulus is similar. Tissue property can be assumed constant across the three species investigated. Whale trabecular bone should be used as a model for human bone only with caution.

CHAPTER 3
MEASURING THE DENSITY AND CROSS-SECTIONAL GEOMETRY OF BONE BASED ON POROSITY USING MAGNETIC RESONANCE IMAGING

3.1 INTRODUCTION

Individuals suffering from skeletal disease such as osteoporosis, benign, or metastatic bone tumors are subject to experiencing fracture under normal loads. In the United States 1.2 million cases of cancer are reported [3], and 60% to 80% of primaries will metastasize to bone [4]. Further 33% to 50% of children are diagnosed with benign bone tumors incidentally [1]. These epidemiological facts coax the need to develop reliable means of determining the fracture risk and utilizing treatment resources to prevent the potential of morbidity and pain.

Measuring material and cross-sectional geometric properties of bone are necessary to determine structural properties. Studies have shown that the stiffness and the strength of normal bone (trabecular and cortical) depend on density [20], and catastrophic failure of bone weakened by metastatic cancer or osteoporosis depend on cross-sectional geometry and density [5]. Therefore, noninvasive methods for predicting failure of pathologic bone must be able to measure both the geometry and density in the bone cross-section.

Dual energy x-ray absorptiometry (DXA) is an inexpensive and precise tool for assessing planar bone mineral density and detecting metabolic bone diseases such as osteoporosis [21]; further it is accurate in measuring cross-sectional properties [22]. Quantitative computed tomography (QCT) is also an accurate tool for densitometry [23] and measuring geometric properties. Both DXA and QCT expose patients to ionizing radiation, approximately 10mr and 2200mr, respectively for a standard bone study. Magnetic resonance imaging (MRI) does not use ionizing radiation and is sensitive to fine changes in tissue pathology. Studies to date that used MRI as a quantitative tool for measuring bone material and mechanical properties have focused on measuring relaxation parameters associated with gradient inhomogeneities created by differences in

the magnetic susceptibility between differing phases of material and its spatial relation [9, 24, 25].

MRI surpasses all imaging modalities in delineating intramedullary abnormalities. It is also better at displaying tumors located on the periphery of the cortex where it can escape detection from plane radiographs, or exhibit poor resolution on CT images [26]. MRI has the unique capability of directly making coronal, sagittal, and transverse cross-sectional slices with the patient in a single position - making it convenient to obtain comprehensive geometric information without repositioning the patient. In general, MRI is often used to determine the nature of osseous lesions, and because it does not emit ionizing radiation it can be used to serially examine patients to monitor the effectiveness of treatment.

Unlike DPA, DXA, or CT which use radioisotope or an *x*-ray energy source, MRI applies principles of magnetism to create images reflecting the dynamic behavior of proton molecules in soft tissue. Our investigation uses differences in the relative signal intensity between soft tissue and bone to measure the porosity of bone (volume of marrow space relative to the bulk volume of the bone). Since bone does not contain appreciable mobile protons it provides insignificant signal, and thus appears black relative to soft tissue.

MRI produces a gray-scale image by measuring the magnetic susceptibility of protons in various constituents as they relax from a perturbed state. Since pore spaces of trabecular bone is filled with hematopoietic (red) or fatty (yellow) marrow, MRI produces a positive image of the interstitial space between trabeculae, and a negative image of the bone matrix. This provides information about the porosity of the bone . Assuming that the tissue properties of bone remains relatively constant [19] with gender and age, apparent or ash density can be determined using the porosity, tissue density, and bone mineral fraction. Similar to QCT, a pixel-mapping algorithm can be created to convert a MR image to a bone density image for determining cross-sectional properties.

The goal of this study was to develop quantitative methods using MRI to measure structural components of bone cross-sections. Excised trabecular specimens from whale vertebral bodies

were used to validate densitometric methods using MRI by comparing measurements with QCT measurements of ash density [8]. The study was furthered extended to compare MRI measurements of bone density and the maximum principal moment of inertia of the distal tibia in human volunteers with QCT measurements. Using MRI to make measurements of structural properties would extend its clinical value by providing information on the load bearing capacity of bone in addition to its prevalent use for imaging soft tissue pathoanatomy.

3.2 Materials and Methods

Ex-vivo and *in-vivo* experiments were conducted to correlate MRI and CT measurements of ash density and maximum principal moment of inertia. In the *ex-vivo* experiment, twelve 12.7mm diameter trabecular specimens were prepared from the vertebral bodies of six whales (*Physeter macrorynchus*, *Baelena mysticetus*, *Koja Breviaceps*) obtained from the North Slope Borough Wildlife Management and National Marine Fisheries. Marrow content was left *in situ* and the specimens were submerged in corn oil. Trapped air within pore spaces was removed using a vacuum chamber. In the *in-vivo* study, transverse scans of the right distal tibia metaphysis above the plafond were obtained from fourteen human individuals (21-79 yrs; 4 females-10 males).

For both the *ex-vivo* and *in-vivo* study, whale specimens and human subjects were examined using a GE high speed helical CT scanner and a hydroxyapatite phantom to convert *x*-ray attenuation to bone ash density. The MRI study was performed using a 1.5T Signa Imager (GE Medical Systems, Milwaukee WI) with a quadragen head coil. Matching images were obtained by cross-referencing a pen-mark on the specimen container for the whale specimens, and the subject's ankle for the tibial metaphysis. A porosity phantom was constructed of one corn oil filled chamber to represent 100% porosity, and three chambers with open-celled polyurethane foam (Quality Foam, Eddystone PA) of different porosity levels (95%, 90%, 85%) to simulate trabecular bone morphology. The foam was immersed in corn oil to simulate the proton

characteristics of yellow marrow [27]. To compensate for axial inhomogeneity of the radio-frequency coils, the phantom was placed next to bone being scanned so that it would be included in each bone slice (Figure 1).

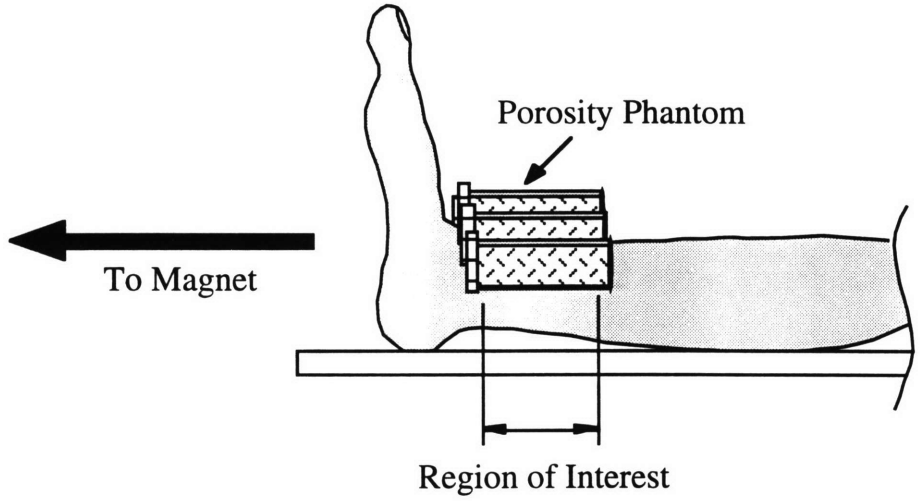

Figure 1 Configuration of Porosity Phantom over Region of Interest to be Scanned

Slice-specific relationships between known porosity and average MR signal intensity of the phantom chambers for serial slices were used as calibration to determine the porosity of selected regions of interest within the bone cross-section.

Depending on the age and location of trabecular structures, pore spaces may be either filled with red or yellow marrow [28,29]. Conversion of red to yellow marrow within long bones of the appendicular skeleton reaches nearly 100% by age 25, and marrow within vertebral bodies remain at about 50% cellularity of red marrow through age 70 [29]. Although the proportionality of water, fat, and protein differ in red and yellow marrow; the density of the protons is about the same. To avoid construction of multiple phantoms to account for the varying proportions of marrow composition, a proton density sequence (TR/TE=5000/18, NEX 2, $0.781^{mm}/_{pixel}$) was used that was relatively insensitive to the differences in proton characteristics between red and yellow marrow. This type of sequence offers a high SNR because the signal is attenuated slightly

by T1 and T2 relaxation processes [33].

Image processing software (Advanced Visual Systems, AVS; Waltham MA) was used to establish the slice specific calibration between known porosity and average MRI signal intensity. The relationship was then used to convert each pixel of the image into a representative volume average bone density (Equation 1).

$$\text{pixel } \rho_{ash} = \left\{(1 - \text{pixel porosity}) * \rho_{tissue}\right\} * \{\text{ash fraction}\} \qquad \textbf{Equation 1}$$

where, ρ_{tissue} = 1.97g/cc (whale); = 1.94g/cc (human, [19])
ash fraction = 0.685 (whale); = 0.399 (human, [19])

The average density and principal moments of inertia for bone tissue above a density threshold was calculated for selected regions of interest.

Bivariate linear correlation analysis was applied to MR versus QCT measurements of density and moment of inertia to determine MRI's ability to perform quantitatively relative to QCT. The *t*-statistic was used to test whether slopes were significantly different from unity.

2.3 RESULTS

A positive and significant linear correlation was found between MRI and CT ash densities for whale vertebra trabecular specimens spanning an ash density range between 0.108g/cc to 0.865g/cc: $\rho_{MRI}=0.934\rho_{CT}$ - 0.001; $r^2=0.986$, $p< 0.01$ (Figure 2). The slope of this linear correlation was not significantly different from unity ($0.2<p<0.5$), and the y-intercept was not statistically significant ($p>0.3$).

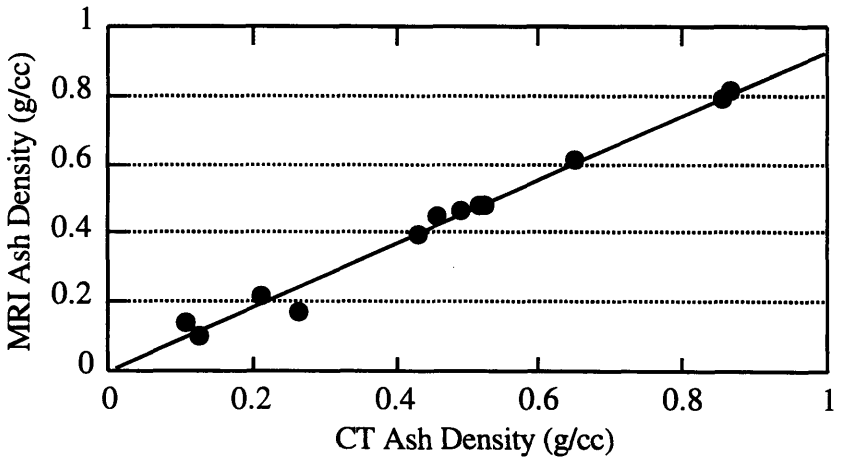

Figure 2 Correlation between MRI and CT Measurements of Ash Density for Whale Trabecular Cores. $\rho_{MRI}=0.934\rho_{CT}-0.001$; $r^2=0.986$ (n=12)

Comparison of bone density at the distal tibia metaphysis assessed using quantitative-MRI and QCT demonstrated a significant positive linear correlation: $\rho_{MRI}=0.658\rho_{CT}-0.001$; $r^2=0.923$, $p< 0.01$ (Figure 3), however the slope was significantly different from unity ($p<<0.05$). The y-intercept was not statistically significant ($p>0.3$).

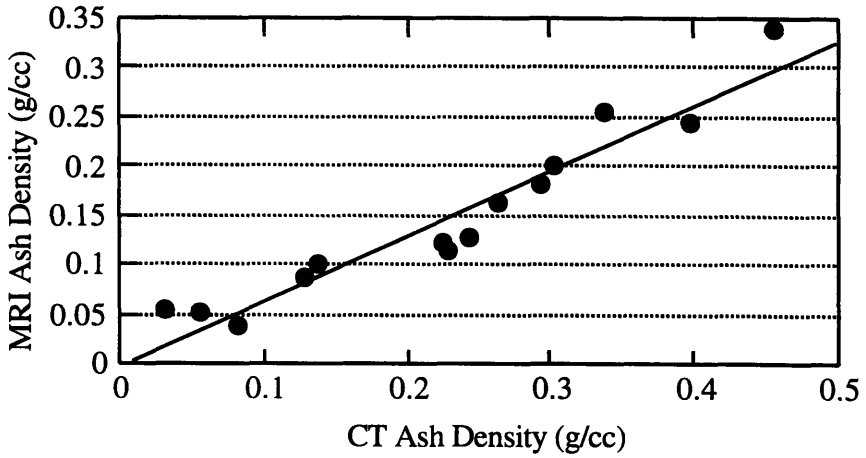

Figure 3 Correlation between MRI and CT Measurements of Ash Density for Trabecular Regions of the Right Distal Tibia. $\rho_{MRI}=0.658\rho_{CT}-0.001$; $r^2=0.923$ (n=14)

Measurement of the maximum moments of inertia using MRI and CT correlated closely for matching cross-sectional images: $I_{MRI}=1.04I_{CT}$ - 0.966; $r^2=0.971$, $p< 0.01$ (Figure 4); the slope was not statistically different from one ($0.1<p<0.2$), and the y-intercept was not statistically significant ($p>0.3$).

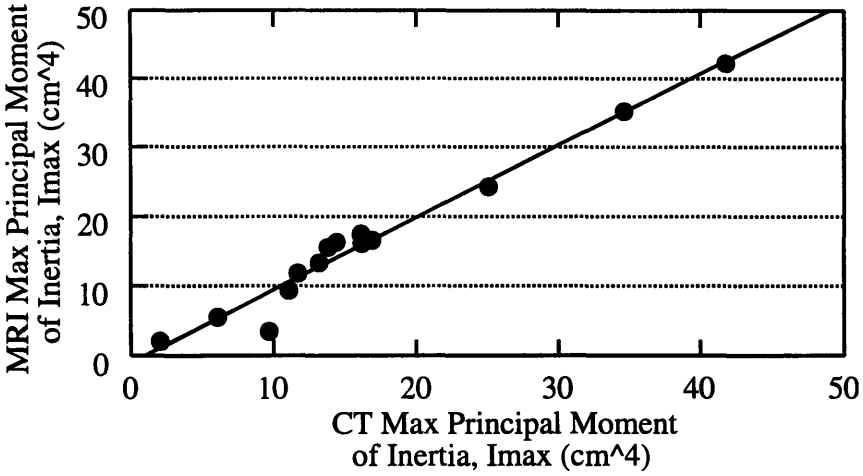

Figure 4 Correlation between Maximum Principal Moment of Inertia Measurements Based on MRI and CT Data for the Right Distal Tibia. $I_{MRI}=1.04I_{CT}$ - 0.966; $r^2=0.971$ (n=14)

3.4 DISCUSSION

Bone density and whole bone cross-sectional geometric properties (principal moment of inertia) measured by MRI using a porosity phantom and a proton density sequence compared well to CT-based measurements using hydroxyapatite phantoms over a broad range of densities in *ex-vivo* and *in-vivo* experiments. The slope for the linear correlation between MRI and CT measurements of density for whale trabecular core specimens was not statistically different from unity. However the slope for the *in-vivo* linear correlation was different from unity. This can be explained by the radial inhomogeneity in the gain field of the head coil. Scanning with the same

proton density sequence, images of a copper sulfate phantom developed by General Electric show a radial decrease in the gain from approximately the center of the coil. Because the region which encompassed the container and phantom for the whale trabecular bone study was small, the variation in intensity within the relevant field of view was insignificant; however for the human study, the position of the porosity phantom and the distal tibia covered a larger FOV, and thus signal inhomogeneity may have influenced porosity measurements. Inaccurate estimation of bone tissue properties may also account for inaccurate measurements of human bone density. MRI based measurements of the second moments agreed with CT measurements because the moment of inertia calculation is based on whether a pixel is within a defined density threshold range, and is less sensitive to the relative density level. Since the inhomogeneity is moderate, our density based algorithm accurately recognizes bone pixels but inaccurately predicts the true density.

Using a porosity phantom, a proton density sequence to homogenize the signal intensity between red and yellow marrow, and the assumption that normal bone consists of constant tissue properties, cross-sectional bone density and geometry can be measured using clinical MR equipment. A broad range in density in two species was investigated in this study. The scan time was less than ten minutes, and is within the typical duration of clinical scans.

In order to correct for inaccurate measurements due to inhomogeneity of the RF coils, a more homogeneous coil must be constructed or a method to correct for the field inhomogeneity must be developed. Proton density MRI measurements of bone density also require an assumption about bone tissue density, we were able to obtain these data from the literature for our healthy human volunteers. Error in MRI-based bone density measurements can be expected if bone tissue density is affected by pathology. Neither MRI nor QCT can distinguish between normal and pathologic bone material. QCT looks purely at x-ray attenuation by bone mineral; it does not discriminate its tertiary structure (*i.e.* woven bone versus lamellar bone which have different mechanical properties). From literature on porous foams, most first order effects, such as strength and stiffness, are explained by bone volume fraction. Both MRI and QCT are adequate for

measuring bone volume fraction - MRI measures porosity then subtracts this from unity, and QCT measures it directly. Therefore no device using *x*-ray as an energy source nor MRI can determine bone quality; each assumes bone material to be normal. MRI has the advantage that it detects small soft tissue changes. Surrounding soft tissues and marrow often reflect bone pathology far earlier than it can be shown on radiographs. Similar to CT, the specificity and sensitivity of applying MRI as a quantitative tool is highly dependent on the ability of the user to accurately identify pathologic and anatomical structures. Osteoblastic tumors which contain few mobile protons will appear similar to bone tissue, however there are extensive MRI sequences which can circumvent this obstacle and assist the user in identifying pathologic regions prior to applying the quantitative technique to predict the structural properties of the bone.

Field inhomogeneity poses the greatest obstacle in measuring bone properties with MRI. Additional work should focus on designing a more homogeneous RF coil suitable for the body section of interest, or implementing an algorithm which corrects for gain differences across the field. With continued advances in NMR technology, applying MRI quantitatively will become more practical; eliminating concerns of field homogeneity, scan duration, and artifact reflection due to pulsatile and patient dynamics.

CHAPTER 4
NONINVASIVE PREDICTION OF FAILURE IN TORSION, BENDING, AND TENSION OF TRABECULAR BONE WITH SIMULATED REGULARLY SHAPED LYTIC DEFECTS USING MAGNETIC RESONANCE IMAGING AND DUAL ENERGY *X*-RAY ABSORPTIOMETRY

4.1 INTRODUCTION

Fractures through various types of skeletal tumors including benign and metastatic cancer and metabolic bone diseases often result in intractable pain, loss of function, and increased morbidity. Benign tumors, such as fibroxanthoma, fibrous dysplasia, aneurysmal bone cyst, and unicameral bone cysts exhibit interstitial bone loss, which result in a decrease in the structural load carrying capacity of the bone. Depending on the applied loads, size, and location of the lesion pathologic fracture may occur. Thirty-three to 50% of asymptomatic children are incidentally diagnosed with benign bone lesions on review of *x*-rays obtained for other purposes [1]. Metastatic bone tumors frequently occur in patients with breast, lung, kidney, thyroid, or prostate cancer [2]. In the United States an alarming 1.2 million new cases of cancer are reported each year [3], and 60% to 80% of these primary tumors will metastasize to bone [4]. In many of the metastatic cases, pathologic fracture results from severe bone loss severely affecting the patients quality of life.

Current clinical guidelines for predicting pathologic fracture in adult and children with benign or malignant tumors are inadequate and have never been proven to be sensitive nor specific. Orthopedic surgeons rely primarily on *qualitative* images from plane radiographs, computed tomography, and magnetic resonance images to assess strength reductions based on defect size, and the presence of pain in the affected bone. Predicting fracture risk is highly dependent on clinical experience. As part of a previous study [5], three orthopedic oncologists were provided radiographs and CT scans of proximal femora with simulated lytic defects and the intact contralateral femur. Each surgeon was asked to predict the relative strength reductions imposed by

the defect. There was no consistency among the physicians in the predicted strength reductions nor correlation with experimentally measured strength reductions. This study demonstrates that experienced orthopedic oncologists cannot reliably predict pathologic fracture risk based on qualitative resources. Currently no objective method for predicting fracture risk associated with osteolytic lesions exists. In an effort to develop a noninvasive, cost-effective method for predicting fracture risk in patients with lytic bone tumors, we investigated three imaging techniques to predict failure in cylindrical cores of trabecular bone with simulated regularly shaped lytic defects. Trabecular bone comprises a majority of the spine and ends of long bones forming joints. Because trabecular bone is metabolically more active than cortical bone, many pathologic activity first appear at sites comprised primarily of trabecular bone. While there have been several studies investigating the effect of holes in cortical bone, to the best of our knowledge there have been no previous studies investigating the effect of holes in trabecular bone. Quantitative assessment of fracture risk will facilitate treatment planning and resource utilization, by providing guidelines for selecting among the various treatment options and monitoring the efficacy of treatment programs.

The microstructure of trabecular bone is similar to other engineering open-cell porous materials [17]; its strength and stiffness vary as power law functions of porosity (or density). Recent studies strongly suggest that trabecular bone fails at a constant strain irrespective of density [30]. Using Euler-Bernoulli composite beam theory we assume that the mechanical behavior of whole bones can be predicted if the cross-sectional geometry and material properties of the bone can be measured. We further assume that the linear elastic behavior of whole bone correlates with the nonlinear, inelastic behavior of the bone at failure [32]. Therefore, assuming that trabecular bone fails at a constant strain, the failure behavior can be predicted from composite beam theory in torsion, bending, and tension (Equations 1-3).

$$T_y = \gamma_y \left(\frac{GJ}{c} \right)$$ **Equation 1**

where, T_y is the applied torque at yield

ε_y is the shear strain at yield

GJ is the bending rigidity at the minimum cross-section along the beam

c is the distance from the centroid to the outer most fiber of the cross-section

$$M_y = \varepsilon_y \left(\frac{EI}{c} \right)$$ **Equation 2**

where, M_y is the applied moment at yield

ε_y is the strain at yield

EI is the flexural rigidity at the minimum cross-section along the beam

c is the distance from the neutral axis to the point of maximum strain of the cross-section

$$F_y = \varepsilon_y (EA)$$ **Equation 3**

where, F_y is the uniaxial load at yield

ε_y is the uniaxial strain at yield

EA is the axial rigidity at the minimum cross-section along the beam

Based on these three equations, we demonstrate that QCT, MRI and DXA, can noninvasively measure the minimum rigidity of trabecular bone rods with and without simulated lytic defects to predict the failure load in torsion, bending, and tension. Circular and slot defects are considered to

assess the effect of two different defect shapes on the structural capacity of the trabecular bone rods. Specimens in this study are symmetric - the distance from the neutral axis to the outer most fiber is the same for all specimens, therefore, yield loads are directly proportional to rigidity. Since failure of a structure depends on the weakest link, the failure load (or couple) for the entire bone is determined predominantly by the minimum cross-sectional rigidity along the length of the bone. It is at the cross-section where rigidity is minimum that most of the deformation occurs for the entire bone. This forms the basis of our algorithm: torsion, bending, and axial rigidities are measured noninvasively at every cross-section through the bone being examined, depending on the applied loading mode, failure occurs at the cross-section where the rigidity is minimum. Since the multiaxial loading of a bone is largely unknown, the reduction in failure load can be predicted by forming the ratio of the minimum rigidity at a cross-section through the bone defect compared to the rigidity at the equivalent cross-section through the intact contralateral bone.

4.2 Materials and Methods

Vertebral bodies from six whale spines were used to obtain homogeneous 12.7mm diameter cores that span a range of densities (ρ_{app}: 0.292g/cc - 1.61g/cc). Circular or slot defects of different sizes were introduced using precise milling equipment. Each specimen was scanned around the defect site with MRI, DXA, and QCT. Specimens were tested to failure in either pure torsion, four-point bending, or uniaxial tension. Regression models were used to relate yield loads to rigidity measurements by each imaging modality.

4.2.1 Specimen Preparation

Trabecular bone from thoracic to caudal vertebral bodies of whale six spines (*Physeter macrorynchus*, *Baelena mystecetus*, *Koja breviaceps*; source: North Slope Borough Wildlife Management and National Marine Fisheries) were used to harvest over two hundred 12.7mm diameter cores. After screening cores for natural discontinuities and irregularities using plane

radiographs, one hundred five specimens were selected for distribution in the study. Large diameter specimens were needed to prepare a range of defect sizes without risking the structural integrity of remaining trabeculae. Specimen cores were embedded in 16mm diameter polymethylmethacrylate endcaps to facilitate mechanical testing and ensure compatibility with MRI (Figure 1).

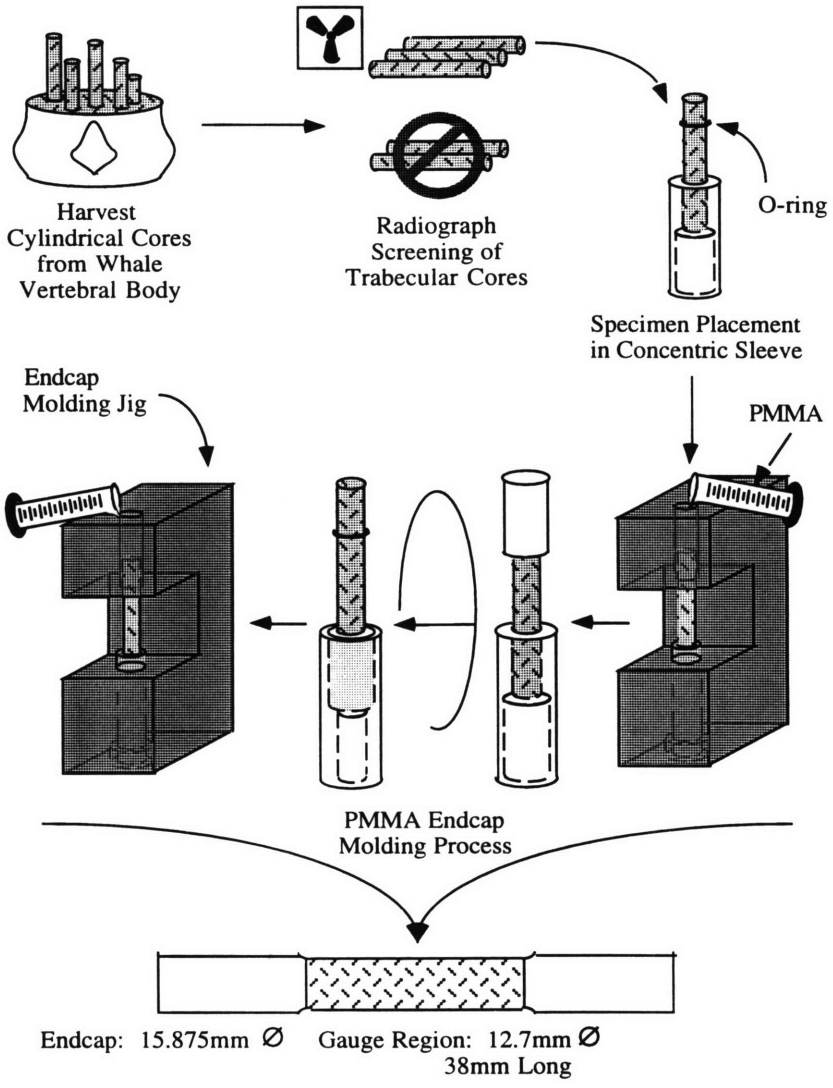

Figure 1 Procedure for Preparing Trabecular Specimens from Whale Vertebral Bodies

Circular and slot defects were created symmetrically at mid-gauge using a Bridgeport mill (Bridgeport CT) and carbide endmill bits (SGS, Munroe Falls OH). Five specimens were randomly distributed to each of seven groupings: one group without any defects, three groups with circular hole diameter to specimen diameter ratio of 28%, 47%, and 56%, and three groups with the same hole to specimen diameter ratios but with a two to one slot length to defect diameter ratio. Thirty-five specimens were prepared for each mechanical testing mode.

4.2.2 Imaging Techniques

4.2.2.1 MRI • For MRI scans, marrow content was left *in situ*, and the specimens submerged in corn oil. Trapped air within pores was removed using a vacuum chamber (Precision, Hingham MA; Labconoco, Kansas City MO). Consecutive 3mm thick transverse images were obtained through the defect site and contiguous bone, using a 1.5T Signa Imager (GE Medical Systems, Milwaukee WI) with a quadragen head coil. A proton density sequence (TR/TE[1] = 5000/18, NEX 2, 0.781mm/pixel) was coded to homogenize the different signal characteristics between hematopoietic (red) and fatty (yellow) marrow (Chapter 3). To obtain quantitative images using MRI, a porosity phantom was imaged with the specimens (Chapter 3). Images were processed using AVS (Advanced Visual Systems; Waltham MA) to convert the signal intensity of each pixel to a representative porosity value using a slice-specific calibration curve between the known porosities and the average MR signal intensities of the phantom chambers. Assuming constant tissue properties [19], the cross-sectional images can be converted to a density map, and used to calculate cross-sectional structural properties. Structural rigidity was estimated by multiplying the cross-sectional polar moment of inertia (J), bending moment of inertia (I), and area (A) of each pixel by an empirically derived density dependent relationship for the shear and elastic moduli, respectively. The rigidity of the entire cross-section was calculated by summing the rigidity of each pixel about the modulus weighted centroid or neutral axis.

---

[1] TR and TE is the repetition time and echo time, respectively.

4.2.2.2 DXA • Specimens were scanned using Hologic's QDR 2000. To simulate soft tissue and to establish a steady baseline, trabecular bone specimens were submerged in water and oriented to obtain cross-sectional measurements perpendicular to the long axis of the specimen. Specimen alignment was maintained with a custom jig. The small animal, high-resolution option was chosen, which emits a pencil beam source at 70KVp and 140KVp synchronously with line frequency [31], and a point resolution of 0.0127cm. Calibration is continuously performed during the scan with a rotating wheel consisting of a bone equivalent material, a soft tissue material, and air [31]. The attenuation at each point is converted bone mineral density (BMD[2]) based on the known attenuation and BMD of the equivalent bone in the calibration wheel (Hologic). A cross-sectional profile of BMD in the plane of the cross-section was generated and used to compute the BMD moment of inertia and area (Figure 2). $I_{yy,BMD}$ and A_{BMD} describe the distribution of bone mineral density in space, similar to a mass moment of inertia as opposed to geometric moment of inertia. Since modulus is a power law function of volumetric density, and planar density is a two dimensional projection of volumetric density, the BMD moment of inertia and area should be proportional to flexural and axial rigidity by a power law relationship.

---

[2] *B*one *M*ineral *D*ensity (BMD) is defined as the mass divided by the projected area, and has units of g/cm^2.

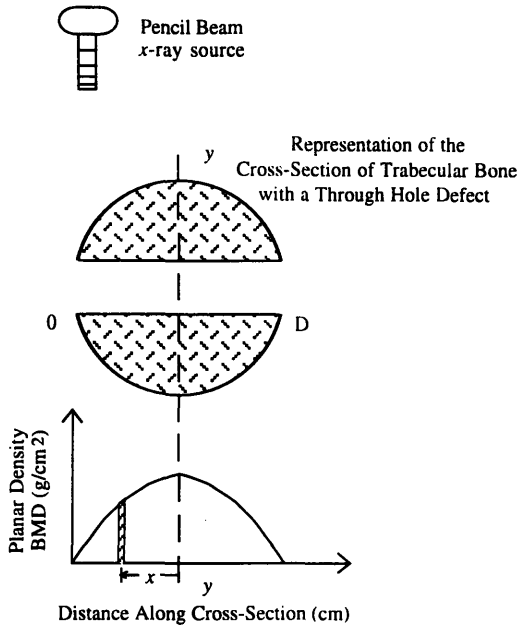

$$I_{yy,\,BMD} = \int_0^D x^2 \, d(BMD)$$

$$A_{BMD} = \int_0^D (BMD)\, dx$$

Figure 2 DXA Measurement of BMD Moment of Inertia and Area

Two mutually perpendicular scans were taken to represent the principal BMD moments of inertia at cross-sections through the defect: one with the defect oriented vertically and another with the defect oriented horizontally. The sum of the moments was the BMD polar moment of inertia.

4.2.2.3 QCT • Specimens were encased in saline filled tubes, and placed in a vacuum chamber to remove air from the pore spaces. A hydroxyapatite phantom was scanned with the specimens in a high speed helical CT scanner (GE Medical Systems, Milwaukee WI). Three millimeter thick slices were taken with a 0.234 mm per pixel resolution. Images were transferred to AVS and converted to bone density images using the hydroxyapatite phantoms[3] (Computerized Imaging Reference Systems, Northfolk VA). Mechanical rigidity (GJ, EI, and EA) of the entire

[3] Measured ash densities of the phantoms are 0.005, 0.0432, 0.142, 0.526, 1.071, and 1.544 g/cm^3.

cross-section was calculated by summing the rigidity of each individual pixel about the modulus weighted neutral axis or centroid.

4.2.3 Mechanical Tests

Specimens were thawed for approximately 25 minutes and tested at 21 °C and 63% relative humidity. Angular, linear, and bending displacements for each testing device were measured using an infrared optical system (MacReflex, Sweden), capable of resolving 3 μm displacements in three dimensional space. One millimeter square infrared (IR) reflective markers were adhered to the specimen, and its relative positions monitored. Load and coordinates of the IR markers were collected synchronously using Biopac (Santa Barbara CA). Failure of the specimens was defined as the yield load which corresponded to the point where the tangent slope of the load displacement curve deviated 30% from the slope of the elastic region.

4.2.3.1 Torsion • The torsion test was performed using a custom built system adapted to a bi-axial servo-hydraulic load frame (Interlaken, Eden Prairie MN) designed specifically to reduce the parasitic forces and moments associated with induced warping of the specimen because of material anisotropy or specimen misalignment (Figure 3).

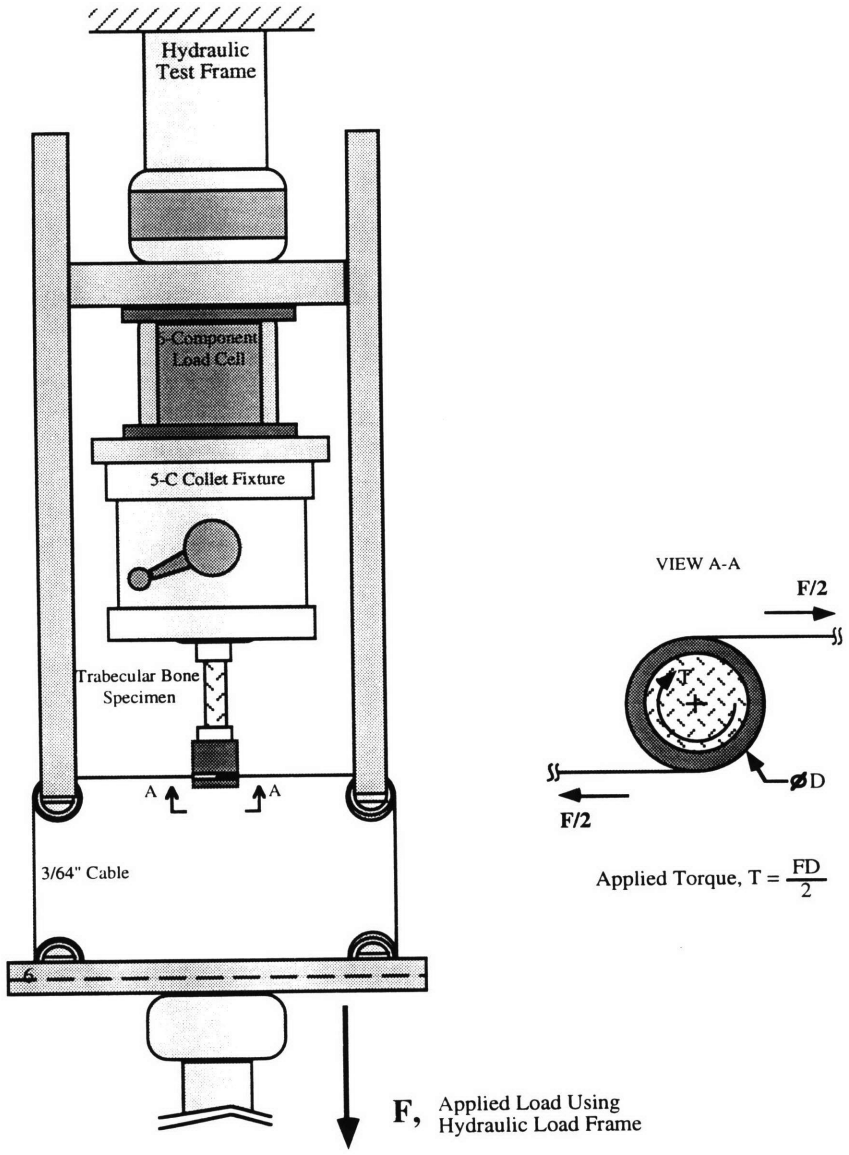

Figure 3 Cable Driven Torsion Apparatus Adapted to a Servohydraulic Load Frame to Reduce Parasitic Loads Due to Specimen Misalignment and Anisotropy

Specimens were affixed at one end with a manual 5-C collet clamp and a steel cable regulated collet at the free end. By applying uniaxial tension, the cable wrapped collet produces a force couple that applies a pure torque. The specimen is unrestricted in its ability to warp out of plane so that no significant parasitic moments or forces are produced. Cast acrylic was chosen to validate the

torsion apparatus because of its similarity to bone stiffness and its machinability. Precision and accuracy of the system were determined by comparing the measured shear modulus of the acrylic cylinder to the calculated shear modulus based on the linear relationship to elastic modulus and Poisson's ratio[4]. Four acrylic rods were turned down to 9.5mm cylinders with a gauge length of 25.4mm to displace approximately fifteen degrees at the maximum breaking strength of the cables. The precision of one acrylic cylinder tested seven times at a strain rate of 0.1%/s was 2.3%/s, and the accuracy of four acrylic cylinders tested once each at the same strain rate was within 4% of the theoretical shear modulus.

Trabecular bone specimens were coated with black ink to reduce IR reflection, and two reflective markers were spaced 25.4mm apart, aligned with the longitudinal axis and symmetric about the defect. Tests were conducted under linear displacement control, with a single ramp to failure at an average strain rate of 0.1%/s. The torsional load was recorded synchronously with the three dimensional positions of the two IR markers at 12Hz. Shear strain between the markers was determined by the product of the relative angular displacement and the ratio between bulk radius to the gauge length[5].

4.2.3.2 Four-Point Bending • A standard four-point bend test was conducted with an apparatus adapted to a uniaxial servo-hydraulic load frame (Instron). Specimens were tested with a 500lb loadcell under displacement control, with a single ramp to failure at a strain rate between 0.05%/s to 0.1%/s. Data was collected at 6Hz. Four markers were placed along the longitudinal neutral axis of the specimen, and used to determine the deflection curve. Instantaneous strain at the minimum cross-section was determined by finding the inverse of the

---

[4] $G = \frac{E}{2(1+\nu)}$

[5] $\varepsilon = \theta \frac{r}{L}$

maximum radius of curvature. Applied moment was determined as the product of half the recorded actuator load and the moment arm (Figure 4).

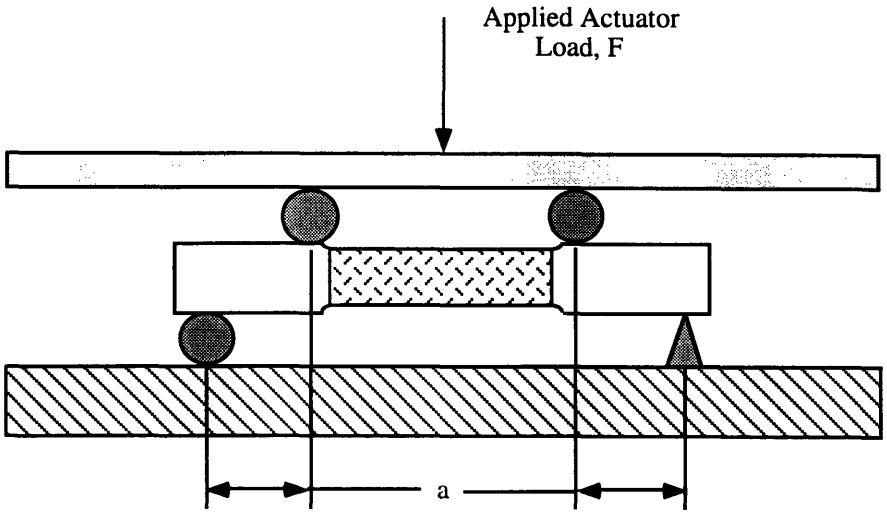

Figure 4 Schematic of Applied Moment on Trabecular Bone Specimen in the Bending Test

4.2.3.3 Uniaxial Tension • Tension tests were also conducted with a system to reduce parasitic loads [32]. Specimens with an apparent density less than 0.44g/cc and defect diameter greater or equal to 47% of the specimen diameter were tested with a 500lb load cell. All other specimens were tested with a 2000lb loadcell. The MacReflex system was used to measure the gauge length displacements. Strain was determined by the ratio of axial displacement over nominal gauge length. Specimens were tested with a single ramp to failure at a strain rate between 0.05%/s to 0.1%/s, and data was collected at 12Hz.

4.2.4 Analysis

Aim 1 - Determine if noninvasive measures of structural rigidity predict failure of trabecular bone specimens with defects. Specimens were grouped according to mechanical testing mode, and a regression applied to yield load (T_y, M_y, and F_y) versus MRI, DXA, and QCT measurements of the prediction model. The coefficient of determination assessed the closeness of

fit, and the p-value provided the significance of the regression. Since DXA cross-sectional measurements is representative of bone mineral density distribution in space, and elastic modulus is a power law function of density, a non-linear regression should also yield good correlation in bending and tension. A two-tailed Fisher's z - test was used to determine if there was a statistical difference between the coefficients of correlation for the two regression models.

Aim 2 - Determine the effect of a circular hole versus a slot on the failure load of trabecular bone specimens. An ANCOVA was used with failure load as the dependent variable, circular hole and slot as the grouping variables, and density and hole width ratio as the covariates.

MRI, DXA, and CT based measurements of rigidity were used to test the ability of noninvasive devices to detect the differences in the load bearing capacity due to defect shape. Specimens were categorized by defect type for each test mode, and a two-tailed Student's t-test was performed to determine the statistical difference between the slope of the regressions due to circular versus slot defects.

Aim 3 - Determine if the reduction in the rigidity predict the reduction in the strength of trabecular specimens with defects. A linear correlation was applied to the relationship between the reduction in the load-bearing capacity and the reduction in noninvasive measurements of rigidity. Load-bearing reduction was defined as the ratio of the measured failure load to the estimated failure load of the specimen before the defect was created. Intact failure was estimated from QCT slice measurements on either side of the defect and an empirical relationship, developed from a subset of specimens, between failure load and QCT measured rigidity. The reduction in rigidity was defined as the ratio of the measured rigidity at the minimum cross-section over the measured rigidity through slices on either side of the defect. The coefficient of determination assessed the closeness of fit, and the p-value provided the significance of the regression.

4.3 RESULTS

Aim 1 - Figures 5 - 7 illustrate the positive linear relationship between the yield load in torsion, four-point bending, and uniaxial tension versus noninvasive measurements of structural rigidity for each imaging modality. Four specimens in the torsion lot and three specimens in the tension lot fractured before being tested. Five specimens were eliminated in the bending lot for the MRI regression because of trapped air within the cross-section with the minimum rigidity. Air has significantly different imaging characteristics, and would cause erroneous porosity measurements. Table 1 shows coefficients of a nonlinear regression model for yield load versus DXA measured rigidity in bending and tension.

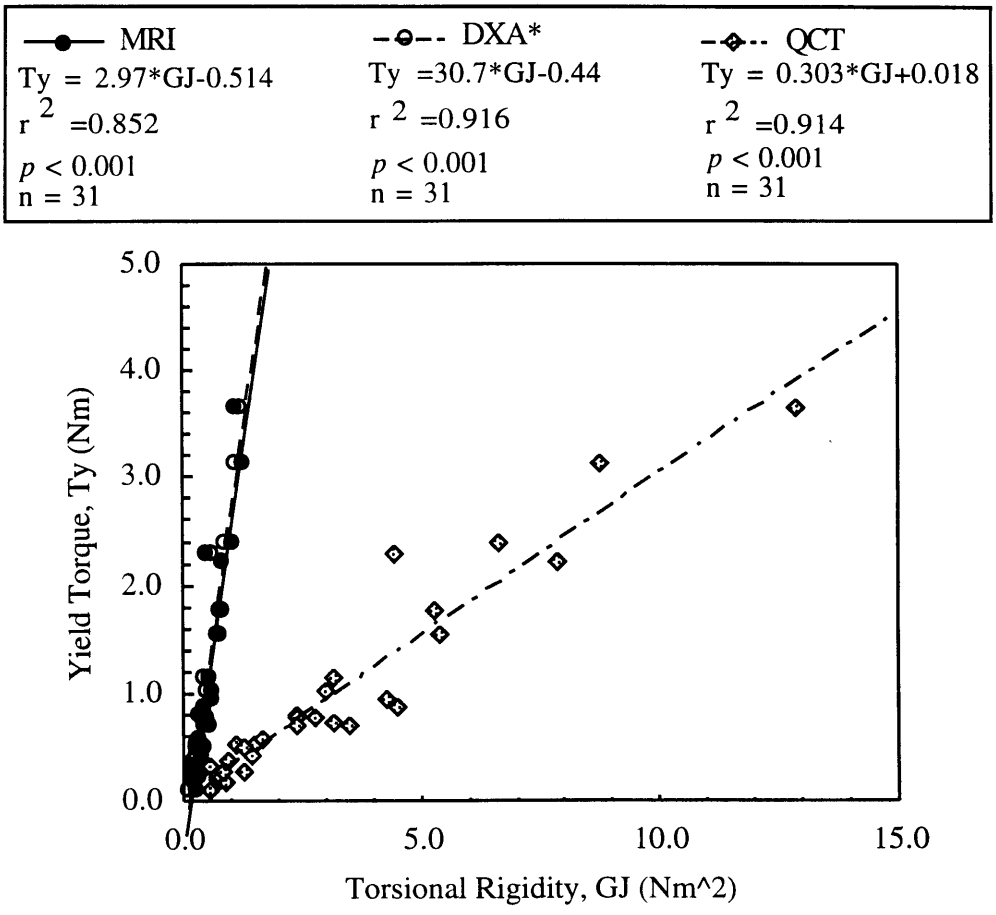

Figure 5 Torsion - Linear Regression between the Yield Torque and Noninvasive

Measurements of Torsional Rigidity (*DXA Rigidity Multiplied by 100. DXA Measures a Planar Density Polar Moment of Inertia and has Units of Grams, g)

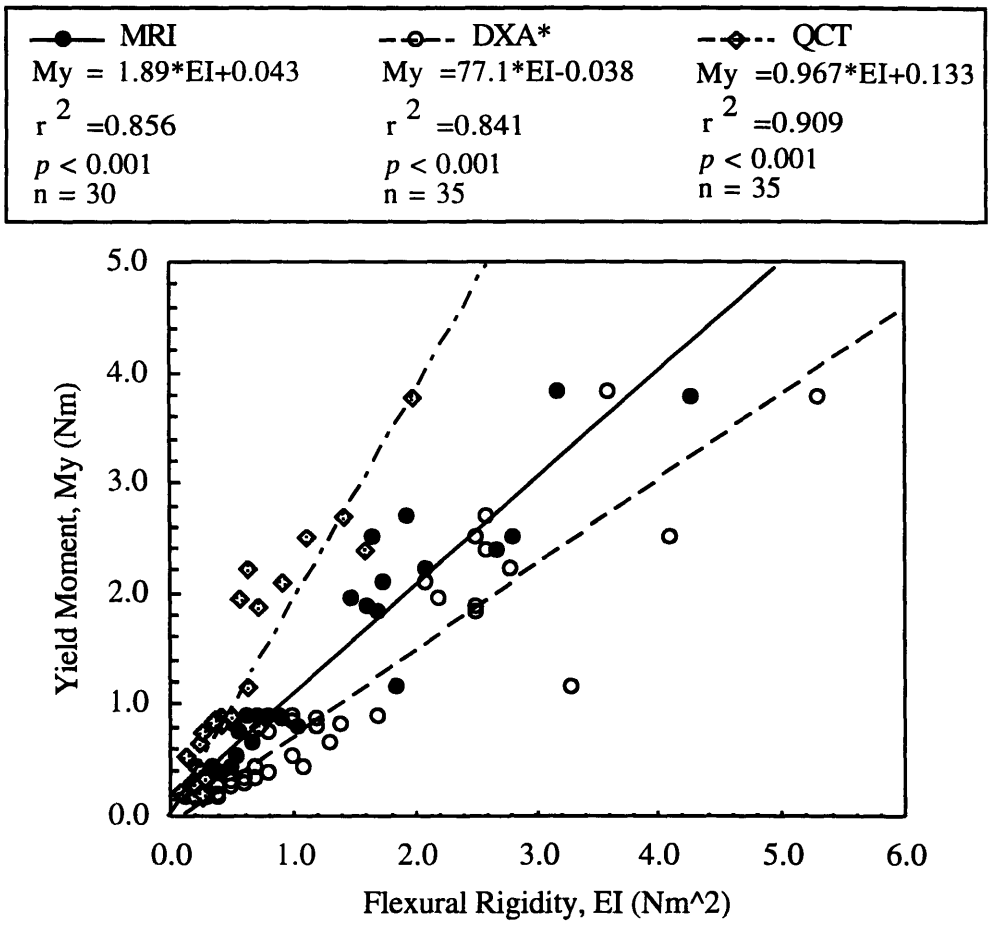

Figure 6 Four-Point Bending - Linear Regression between the Yield Moment and Noninvasive Measurements of Flexural Rigidity (*DXA Rigidity Multiplied by 10. DXA Measures BMD Moment of Inertia and has Units of Grams, g)

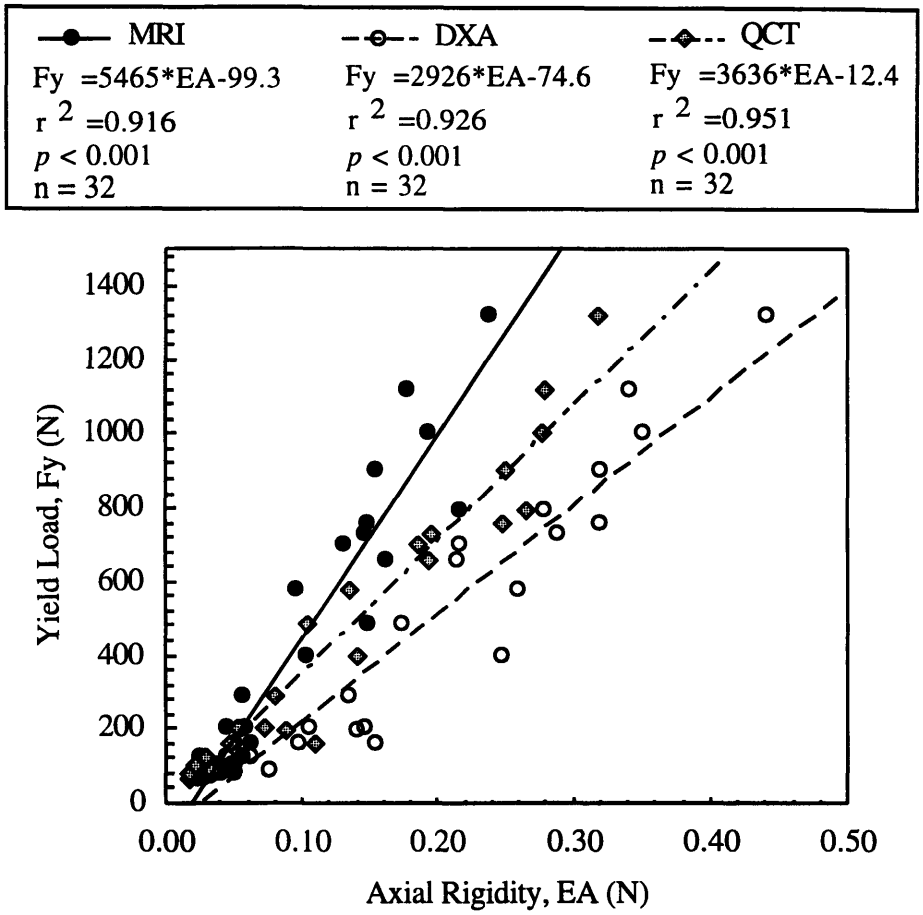

Figure 7 Tension - Linear Regression between the Yield Load and Noninvasive Measurements of Axial Rigidity

Table 1 Summary of Correlations Using Nonlinear Regression Model for Failure Load in Bending and Tension versus DXA Measurements of Rigidity

Nonlinear Regression Model (y = *a* x^*b* + *c*)						
Imaging Mode	Mechanical Test Mode	*a*	*b*	*c*	r^2	*p* - value
DXA	Bending	41.0	0.77	-0.409	0.849	< 0.001
	Tension	4461.8	1.48	37.2	0.944	< 0.001

Results from a Fisher's *z*-test indicated there were no statistical difference in the coefficients of

correlation for the linear and nonlinear models (z>0.50).

Aim 2 - Results from analysis of covariance showed that there was a significant difference due to defect shape in the mean failure load for torsion (H_o: $\mu_1 = \mu_2$; $p = 0.006$), but not in bending ($p = 0.710$) and tension ($p = 0.219$). Table 3 presents the outcome of using noninvasive methods to detect differences in the failure load due to defect shape. The slopes of regressions between failure load and rigidity were inconsistently affected by defect shape.

Table 3 Student's t-test on Linear Regression Slopes to Determine the Effect of Circular Hole versus Slot on the Failure of Trabecular Bone Based on Noninvasive Measurements of Rigidity

Imaging Mode	Mechanical Test Mode	ε	Slope	r^2	Student's t -test on Slopes
MRI	Torsion	1	2.50	0.717	$p < 0.05$
		2	3.50	0.913	
	Bending	1	2.00	0.918	$p > 0.20$
		2	1.72	0.538	
	Tension	1	6148.8	0.951	$p < 0.05$
		2	4673.1	0.890	
DXA	Torsion	1	29.68	0.875	$p > 0.20$
		2	31.70	0.958	
	Bending	1	104.2	0.925	$p > 0.20$
		2	99.2	0.954	
	Tension	1	3277.4	0.953	$p < 0.05$
		2	2691.6	0.934	
QCT	Torsion	1	0.37	0.920	$p < 0.05$
		2	0.29	0.982	
	Bending	1	1.32	0.949	$p < 0.05$
		2	1.07	0.957	
	Tension	1	3794.2	0.983	$p < 0.05$
		2	3199.3	0.938	

Aim 3 - Reduction in the failure load for defect specimens was estimated by taking the ratio of the mechanically tested failure load over the failure load estimated using an empirical relationship between failure load and QCT measured rigidity of an intact cross-section. Table 4 presents the coefficients of determination and the significance of linear correlations for the reduction in failure load versus the reduction in rigidity by virtue of the defect.

Table 4 Summary of r^2 for Estimated Reduction in Failure Load versus Reduction in Rigidity

Linear Regression Model			
Imaging Mode	Mechanical Test Mode	r^2	*p* - value
MRI	Torsion	0.608	< 0.001
	Bending	0.677	< 0.001
	Tension	0.709	< 0.001
DXA	Torsion	0.773	< 0.001
	Bending	0.822	< 0.001
	Tension	0.842	< 0.001
QCT	Torsion	0.706	< 0.001
	Bending	0.804	< 0.001
	Tension	0.828	< 0.001

4.4 DISCUSSION

The use of beam theory to derive the proportional relationships between failure in torsion, bending, and tension to structural rigidity assumes that trabecular bone fails at a constant independent of strain density, and that the distance between the centroid or neutral axis to the outer most fiber of the cross-section is constant for all specimens. This model also implies that structural behavior is not significantly influenced by stress concentrations at the continuum level. The strong relationship between failure load and rigidity demonstrate that the failure of specimens without simulated defects and those with circular and slot defects can be predicted by the minimum rigidity of the bone structure measured noninvasively by MRI, DXA, and QCT.

Although it was expected that a nonlinear (power law) regression model would better relate failure load to DXA measurements of rigidity, a Fisher's *z*-test showed there was no significant difference between coefficients of correlation between the linear and nonlinear regressions ($z>0.50$).

For the defect sizes and shapes in our study, the failure behavior of trabecular bone in torsion is affected differently by a circular hole versus a slot, however the effect of defect shape cannot be consistently detected by using noninvasive measurements of rigidity. Noninvasive measurements of rigidity is not enough to comprehensively describe the failure behavior of an

entire structure or distinguish the differences in the mechanical behavior of specimens with different defect shapes. However variation in the rigidity at the minimally rigid cross-section does predict greater than 85% of the variation in yield load for cylindrical trabecular specimens, indicating that the influence of defect shape is minimal compared to the overall minimum rigidity for the type and range of defect sizes used in this study. To further understand the effect of defect length compared to defect width, another study would have to be conducted varying the length of the slot.

Benign and metastatic tumors of long bones reside predominantly in trabecular regions. If the failure of composite whole bone is consistent with trabecular bone, and failure can be predicted by simple models in torsion, bending, and tension, then relative fracture risk for a predominant loading condition can be defined as the ratio between the rigidity of the pathologically affected bone compared to the rigidity of the contralateral intact bone. Correlations in this study between the reduction in failure load versus the reduction in rigidity were performed by estimating the failure load of the specimen containing the defect as if it were intact using an empirical relationship between failure and rigidity of a small subset of trabecular specimens not containing any defect. The correlations substantiate that a relationship exists between a reduction in failure load and a reduction in rigidity. By defining fracture risk in this manner, individual load-bearing requirements must also be considered in the treatment plan. Even though two individuals may have similar reductions in rigidity, they may load their bones differently and will not be at the same risk for fracture. This definition provides the relative fracture risk between contralateral limbs.

Quantitative computed tomography (QCT) has been shown to accurately measure material [8] and structural properties of bone, predictors of mechanical properties [5,20]. Magnetic resonance imaging (MRI) and dual energy x-ray absorptiometry (DXA) have also proven promise in predicting fracture [9,10]. The use of QCT examinations cost approximately $500, and expose the patient to approximately 2200mr of ionizing radiation for a standard bone study. This is forty times the radiation dosage of a standard chest x-ray. Typical DXA scans expose patients to 10mr of

radiation, and MRI uses no ionizing radiation. The cost associated with a DXA scan is relatively low, but the cost of a MRI exam is nearly twice the amount for QCT; however, MRI is best at identifying fine changes in pathologic tissue.

Current quantitative methods using MRI to relate the strength of trabecular bone to changes in the transverse relaxation time are limited to pathologic cases resulting from solely a decrease in apparent bone density. These methods cannot be applied to cases where a substantial portion of bone is lysed due to tumor growth.

Varying signal intensity over a field of a common substance is due to the inhomogeneity of the RF coil - this poses the most obstinate obstacle in the MRI protocol used in this study. A self-correcting algorithm or a post-processing correction factor must be applied to reduce errors associated with field inhomogeneity. Similar to CT, the specificity and sensitivity of applying MRI as a quantitative tool is highly dependent on the ability of the user to accurately identify pathologic and anatomical structures. Osteoblastic tumors which contain few mobile protons will appear similar to bone tissue, however there are extensive MRI sequences which can circumvent this obstacle and assist the user in identifying pathologic regions prior to applying the quantitative technique to predict the structural integrity of the bone. In general, MRI's non-radiative nature and superior capability to delineate soft tissue pathology will make it a useful tool to serially exam patients and to determine the efficacy of treatment in patients with bone defects.

With the DXA algorithm and post-processing techniques used in this study, it is not possible to directly measure cross-sectional geometry of trabecular bone. However, second moments of the BMD cross-sectional profile provide an analogous form of a modulus weighted moment of inertia. Because of the density weighting, it was expected that failure load would nonlinearly correlate with the BMD second moments. Data illustrate a slight power law function, and the nonlinear regression model showed a higher coefficient of determination for both bending and tension, but since the power coefficient was not strong there was not a statistical difference in the predictive power of the nonlinear (power law) function over the linear function.

DXA's low ionizing radiation and economic cost make it an attractive quantitative tool. Its current use as a tool for diagnosing osteoporosis have made DXA machines readily available, and can now be extended to predict the risk for fracture of bone with benign or metastatic tumors. The operation of DXA machines and the lack of hardware mobility make it difficult to obtain measurements about a structure's predominant loading axis, therefore finding multiple moments of inertia about a common axis presents a challenge, however for conditions where uniaxial tension or compression is the predominant mode of loading, single slices are sufficient to provide the equivalent estimate of axial rigidity.

Current clinical methods that rely on measuring defect size from qualitative images account for geometry only. According to beam theory, the mechanical behavior of a structure is dependent on both material and geometric properties. By taking advantage of imaging techniques to measure bone mineral or porosity and cross-sectional geometry, structural properties can be estimated and used as a measure to predict fracture. Each imaging modality has its strengths and weaknesses, and its selection can be determined by the compatibility with other diagnostic tests and equipment availability.

REFERENCES

1. Sileverman; Essentials of Caffey's Pediatric *X*-ray Diagnosis; *Pediatric Radiology* 1989, 1216.
2. Wiesel SW, Delahay JN, Connell MD; *Essentials of Orthopedic Surgery*; WB Saunders Company, 1993.
3. Wingo PA, Tong T, Bold S; Cancer Statistics; *CA Cancer Journal Clinics* 1995, Vol 45, p 8.
4. Berrettoni B, Carter J; Current Concepts Review: Mechanisms of Cancer Metastasis to Bone; *Journal of Bone and Joint Surgery* 1986, Vol 68A, pp 308-312.
5. Hipp JA, Springfield DS, Hayes WC, Predicting Pathologic Fracture Risk in the Management of Metastatic Bone Defects, *Clinical Orthopaedics and Related Research* 1995, No 312, pp 120-135.
6. ASTM E143-87; Standard Test Method for Shear Modulus at Room Temperature; *ASTM*, pp 283-286.
7. Carter DR and Hayes WC; Bone Compressive Strength: The Influence of Density and Strain Rate; *Science* 1976, pp 1174-1176.
8. Fritz SL, Stockham SD; Validation of Quantitative Computed Tomographic Evaluation of Bone Mineral Density of Several CT Scanners; *SPIE* 1992, Vol 1652, pp 304-309.
9. Chung H, Wehrli FW, Williams JL, Kugelmass SD; Relationship between NMR Transverse Relaxation, Trabecular Bone Architecture, and Strength; *Proceedings National Academy of Science* 1993, Vol 90, pp 10250-10254.
10. Myers ER, Hecker AT, Rooks DS, Hipp JA, Hayes WC; Geometric Variables from DXA of the Radius Predict Forearm Fracture Load *In Vitro*; Calcified Tissue International 1993, Vol 52, pp 199-204.
11. Keller TS; Predicting the Compressive Mechanical Behavior of Bone; *Journal of*

Biomechanics, MS#92-191 Rev 1.

12. Rho JY, Hobatho MC, and Ashman RB; Relations of Mechanical Properties to Density and CT Numbers in Human Bone; *Medical Engineering Physics* 1995, Vol 17, pp 347-355.

13. Kuhn JL, Goldstein SA, Ciarelli MJ, and Matthews LS; The Limitation of Canine Trabecular Bone as a Model for Human: A Biomechanical Study; *Journal of Biomechanics* 1989, Vol 22, pp 95-107.

14. Klever FJ, Klumpert R, Horenberg J, Grotenboer JH, Van Campen DH, and Pauly T; Global Mechanical Properties of Trabecular Bone: Experimental Determination and Prediction from Structural Model; *Biomechanics: Current Interdisciplinary Research* SM Perren, E Schneider, eds. Martinus Nijhoff: The Netherlands, 1985, pp 167-172.

15. Harrigan TP, Oh I, Harris WH, Mann RW, and Carter DR; The Anisotropic Properties of Trabecular Bone; *Proc 6th NE Bio-Engineering Conference* 1980, pp 5-10.

16. Carter DR and Hayes WC; The Compressive Behavior of Bone as a Two-Phase Porous Structure; *Journal of Bone and Joint Surgery* 1977, Vol 59A, pp 954-962.

17. Gibson LJ, Ashby MF; *Cellular Solids Structures and Properties*, Pergamon Press, 1988.

18. Ford CM, Keaveny TM; The Dependence of Shear Failure Properties of Trabecular Bone on Apparent Density and Trabecular Orientation; *Journal of Biomechanics* 1996, Vol 29, No 10, pp 1309-1317.

19. Cowin SC; *Bone Mechanics*, CRC Press Inc, 1989.

20. Rice JC, Cowin SC, Bowman JA; On the Dependence of the Elasticity and Strength of Cancellous Bone on Apparent Density; *Journal of Biomechanics* 1988, Vol 21, No 2, pp 155-168.

21. Satoshi H, Yang S, Gluer CC, Bendavid E, Genant, HK; Noninvasive Bone Mineral Density Measurement in the Evaluation of Osteoporosis; *Osteoporosis* 1994, Vol 20, No 3, pp 651-669.

22. Martin RB, Burr DB; Noninvasive Measurement of Long Bone Cross-Sectional Moment

of Inertia by Photon Absorptiometry; *Journal of Biomechanics* 1984, Vol 17, No 3, pp 195-201.

23. Satoris DJ, Resnick D; Current and Innovative Methods for Noninvasive Bone Densitometry; *Orthopedics* 1990, Vol 28, No 2, pp 257-278.

24. Grampp S, Majumdar S, Jergas M, Lang P, Gies A, Genant HK; MRI of Bone Marrow in the Distal Radius: *in-vivo* Precision of Effective Transverse Relaxation Times; *European Radiology* 1995, Vol 5, pp 43-48.

25. Jergas MD, Majumdar S, Keyak JH, Lee IY, Newitt DC, Grampp S, Skinner HB, Genant HK; Relationships between Young Modulus of Elasticity, Ash Density, and MRI Derived Effective Transverse Relaxation T2* in Tibial Specimens; *Journal of Computer Assisted Tomography* 1995, Vol 19, No 3, pp 472-479.

26. Unni KK; *Bone Tumors;* Churchill Livingstone, 1988.

27. Mulkern RV, Meng J, Bowers JL, Oshio K, Zuo C, Li H, Williamson DS, Jaramillo D; *In vivo* Bone Marrow Lipid Characterization with Line Scan CPMG Proton Spectroscopic Imaging; *Magnetic Resonance Imaging*; Submitted November 1996.

28. Moore SG, Dawson KL; Red and Yellow Marrow in the Femur: Age-Related Changes in Appearance at MR Imaging; *Radiology* 1990, Vol 175, pp 219-223.

29. Vogler III JB, Murphy WA; Bone Marrow Imaging; *Radiology* 1988, Vol 168, pp 679-693.

30. Ford CM, Keaveny TM; The Dependence of Shear Failure Properties of Trabecular Bone on Apparent Density and Trabecular Orientation; *Journal of Biomechanics* 1996, Vol 29, No 10, pp 1309-1317.

31. Wahner HW, Fogelman I; *The Evaluation of Osteoporosis: Dual Energy X-ray Absorptiometry in Clinical Practice*; Mayo Foundation and Ignac Fogelman, 1994.

32. Cabe GD; *Noninvasive Measurement of Load Capacity of Trabecular Bone with Defects*; Thesis, Massachusetts Institute of Technology, 1997.

33. Stoller DW; *Magnetic Resonance Imaging in Orthopaedics and Sports Medicine*; Lippincott, 1993.

APPENDIX A
DESIGN AND VALIDATION OF ANTI-PARASITIC LOAD TORSION APPARATUS

A.1 OBJECTIVE

Anisotropic materials that do not have a torsional axis collinear with the torsional system is subjected to combined loading. Under standard torsion devices, a test material is fixed at the two ends, and the material is constrained from displacing freely due to parasitic loads. This constraint causes the heterogeneous stress distribution along the axis of the material.

A.2 CONCEPT

By adapting a compliant cable system to a uniaxial hydraulic load frame, pure torque can be applied to a material by allowing displacement due to parasitic loads.

A.3 SCHEMATICS AND PRINTS

A.3.1 Parts List

PN	Part Description
1.	Side Panels
2.	Load-Frame Base Plate
3.	MC3A-6-100, 6-Component Load Cell (AMTI)
4.	Load Cell/ Clamp Connection Plate
5.	Manual 5-C Collet Fixture, $1\frac{1}{8}$" (Eagle Rock Technologies)
6.	Cable Plate
7.	Specimen Collet
8.	Trabecular Bone Specimen

9. Cable Bar

10. B-812 (Torrington), Needle Frictionless Bearing

11. Bearing Sleeve

12. Cable, 7x19 Strand Core Wire Rope, 3/64" diameter (McMaster-Carr)

13. Interlaken Series 3300, Hydraulic Load-Frame

*Not shown in following prints is a MCA 6-component amplifier (AMTI).

A.3.2 Assembly

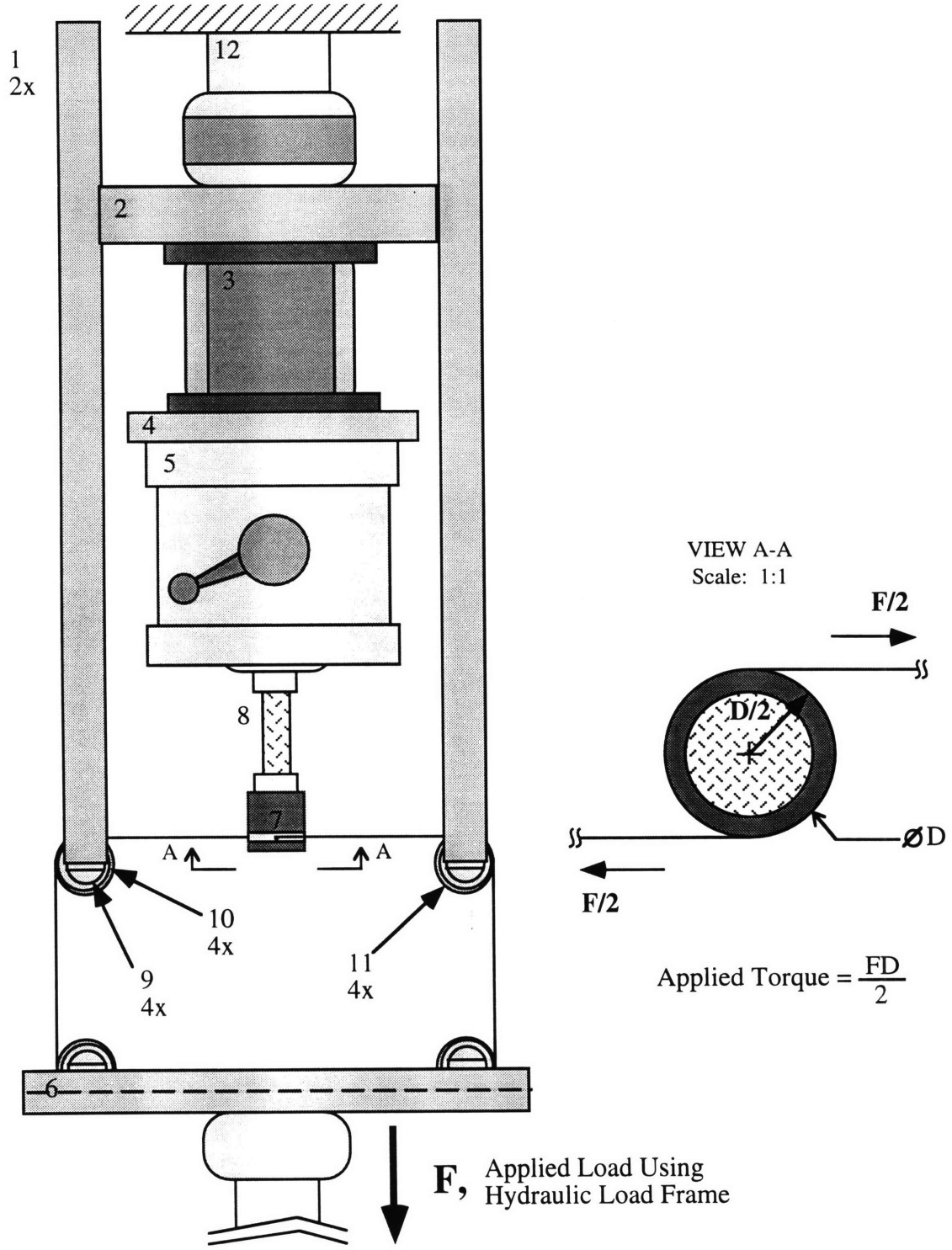

Assembly: Cable-Driven Torsion Apparatus
Scale: ~1:3

A.3.3 PN 1 Side Panels

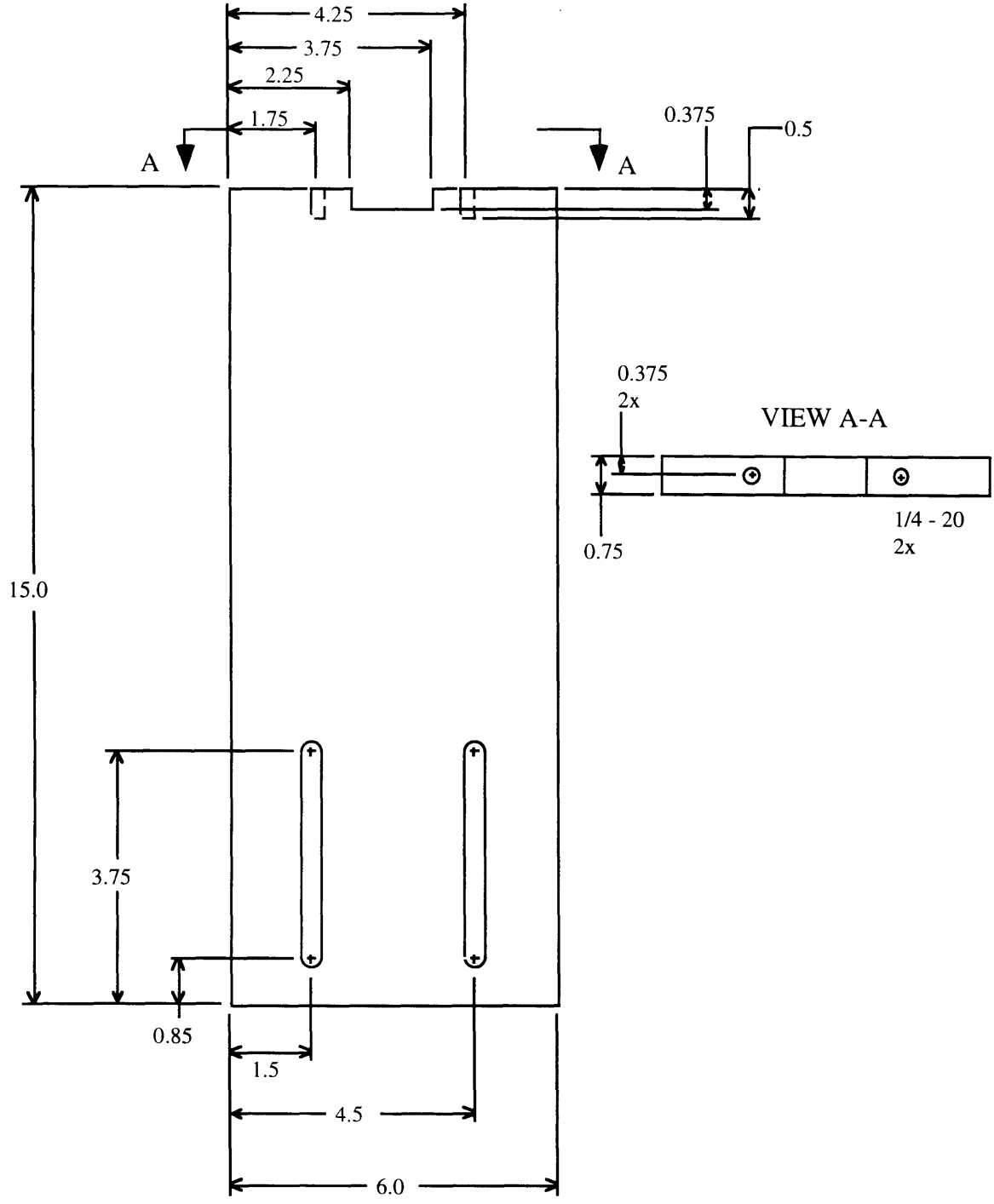

Piece Unit 1: Side Panels
Scale: 1:3
Dimensions: Inches
Material: Aluminum
Quantity: 2

A.3.4 PN 2 Load-Frame Base Plate

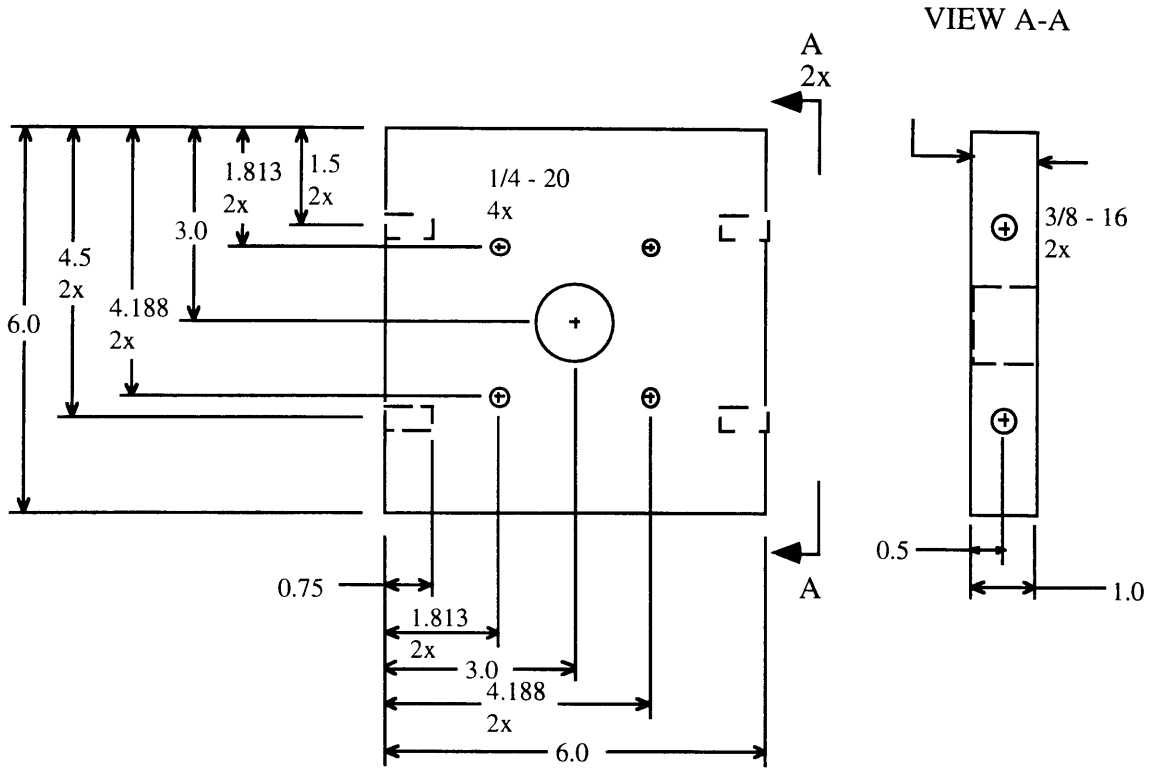

Piece Unit 2: Load-Frame Base Plate
Scale: 1:3
Dimensions: Inches
Material: Aluminum
Quantity: 1

A.3.5 PN 4 Load-Cell/ Clamp Connection Plate

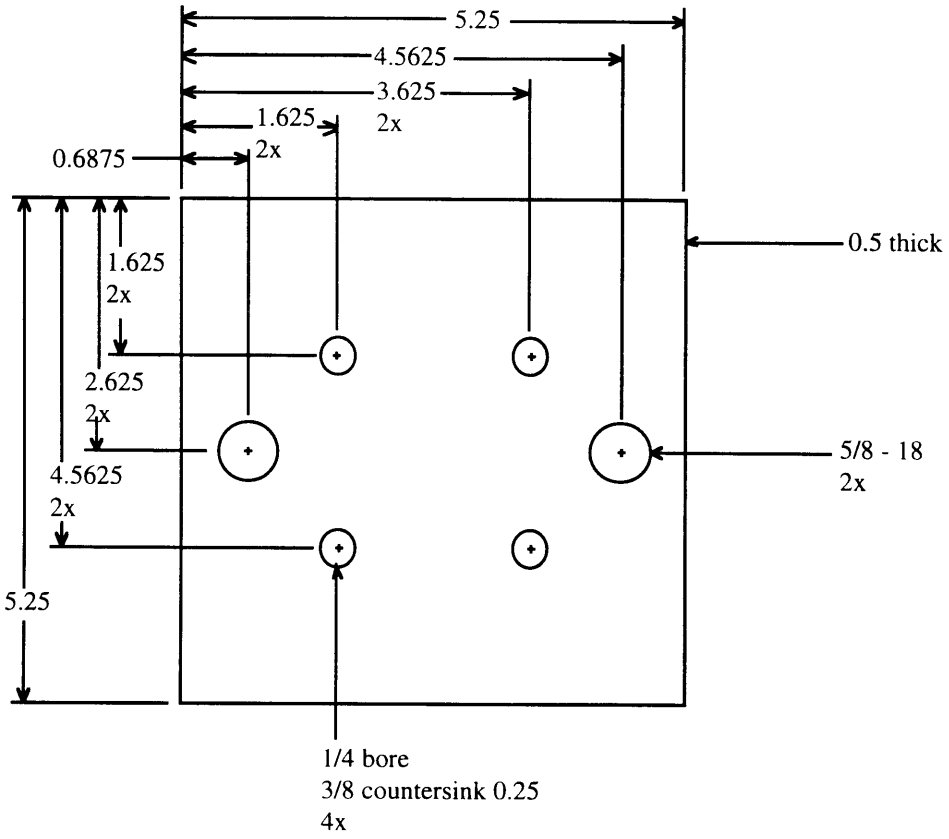

Piece Part 4: Load-Cell/Clamp Connection Plate
Scale: 1:2
Dimensions: Inches
Material: Aluminum
Quantity: 1

A.3.6 PN 6 Cable Plate

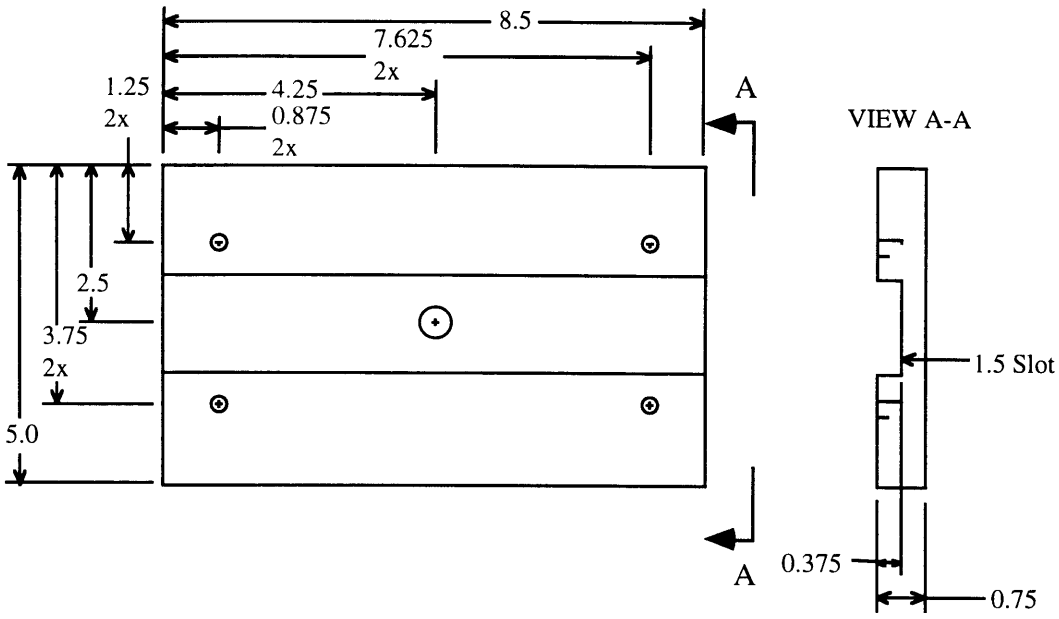

Piece Unit 6: Cable Plate
Scale: 1:3
Dimensions: Inches
Material: Aluminum
Quantity: 1

A.3.7 PN 7 Specimen Collet

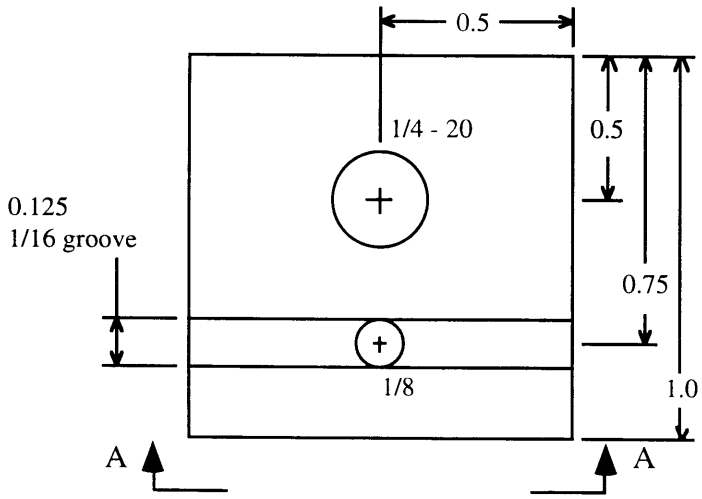

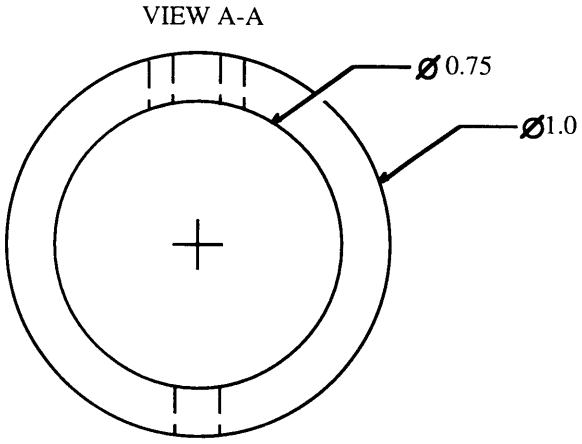

Piece Unit 7: Specimen Collet
Scale: 2:1
Dimensions: Inches
Material: Aluminum
Quantity: 1

A.3.8 PN 9 Cable Bar

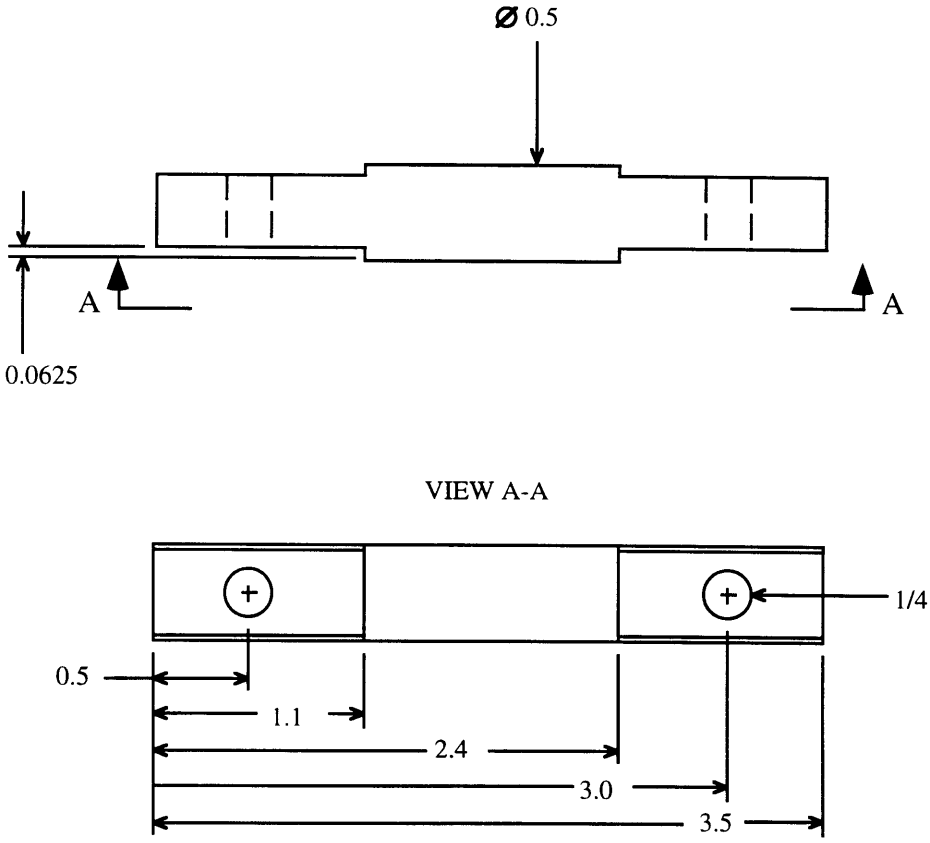

Piece Unit 9: Cable Bar
Scale: 1:1
Dimensions: Inches
Material: Aluminum
Quantity: 4

A.3.9 PN 11 Bearing Sleeve

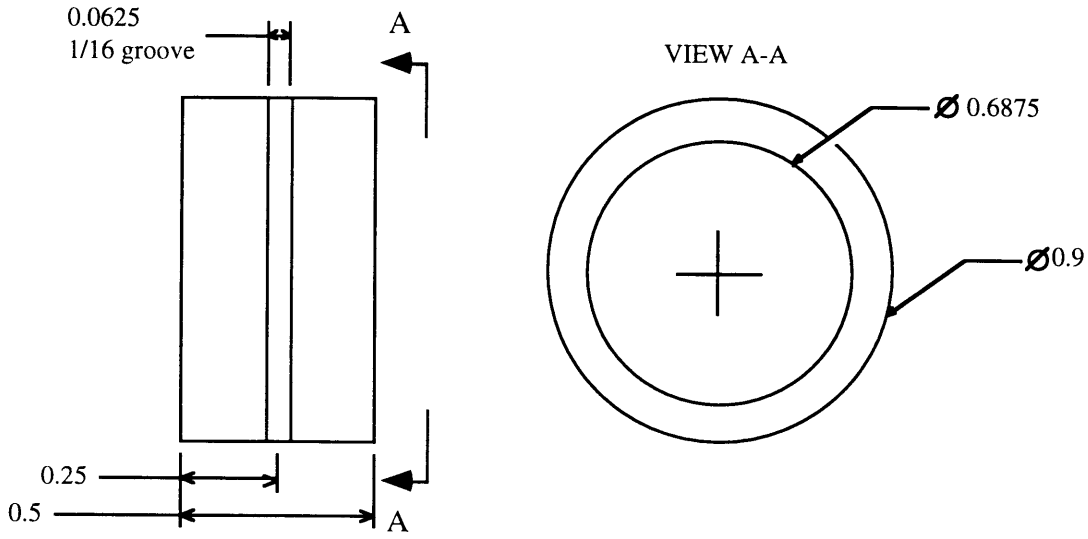

Piece Unit 11: Bearing Sleeve
Scale: 2:1
Dimensions: Inches
Material: Aluminum
Quantity: 4
Note: Groove not shown in VIEW A-A

A.3.10 Calculations for Screw Selection

Calculations

Screw Selection for Screws on Bearing Plates

Anticipated Torsional Strength of trabecular bone is 4Nm (mature bone head)

$n = 2.5$ (safety factor)

$T = 4\,Nm \times 5 = 20\,Nm \times \frac{lb}{4.448\,N} \times \frac{39.37\,in}{1\,m} = 177.02\,lb\cdot in$

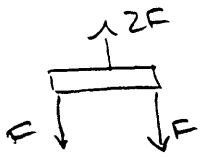

Anticipating a 1 inch coupling ring, the moment arm is $R = 0.5\,in$

Applied Axial Load

$$I = \frac{T}{R} = \frac{177.02\,lb\cdot in}{0.5\,in} = 354.044\,lb$$

$2F = 708.1\ lb$

First selection use 1/4" screw

From _Mechanical Engineering Design_ p. 380 proof strength is 33 Kpsi for low-medium carbon steel screws

Tensile stress:

$$\sigma_T = \frac{F}{\text{Tensile stress area}} = \frac{354.044\,lb}{0.0318\,in^2}$$

(p. 361 $A = 0.0318\,in^2$)

$\sigma_T = 11133\,psi \Rightarrow 11.1\,ksi < 33\,ksi$

Use 1/4-20 ←

Screw Selection for Screws on Multiaxial Load-Cell Plate

$$\tau = \frac{2F}{\pi d_r h} \quad (p.367)$$

Minor Area for 1/2" screw (p. 361) $= 0.0678\,in^2$

$$d_r = \left(\frac{4A_r}{\pi}\right)^{1/2} = 0.2938$$

$$\tau = \frac{2 \times 354.044\,lb}{\pi} \times \frac{1}{0.2938} \times \frac{1}{0.5\,in} = 4819.9\,psi$$

↖ anticipated

$\tau = 4.82\,Ksi$

use 3/8-16 ←

Upper Platform

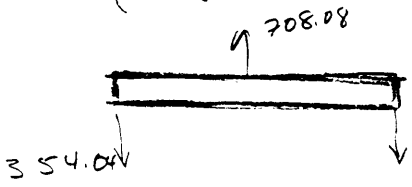

Plate thickness 0.375in

$\sigma = \frac{Mc}{J}$ $\qquad \frac{c}{J} = \frac{h/2}{bh^3/12}$

$M = 354.04\,lb \times (4\,in) = 1416.16\,lb\,in$

$h = 0.375$ $\qquad \frac{c}{J} = \frac{1}{2} \cdot 0.375in \times 12 \times \frac{1}{5in \times (0.375in)^3} = 8.53$

$\sigma = 1416.16\,lb\,in \times 8.53 = 12084.6\,psi \Rightarrow 12.1\,ksi$

$h = 0.625$ $\qquad \frac{c}{J} = 3.072 \Rightarrow \sigma = 4350.4 \Rightarrow 4.35\,ksi$
$1 - 0.375"$

Admiral Metals - Standard Al is 6061
YS ≈ 40 ksi

use 3/4 inch Al plate ←

Bearing Rod

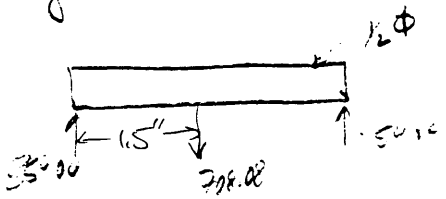

$M = 354.04\,lb \times (1.5\,in) = 531.06\,lb\,in$

$\frac{c}{J} = \frac{d/2}{\pi d^4/64} = \frac{0.5}{2} \times 64 \times \frac{1}{\pi(0.5)^4} = 81.5$

$\sigma = \frac{Mc}{J} = 43224.7\,psi \Rightarrow 43.3\,ksi$

use 3/4 in threaded rod ←

Iculation

Is 3/8-24 UNF (thread) steel strong enough for torsion tests

p.368 (Mechanical Engr Design)

$$\sigma = \frac{-4pF}{\pi h(d^2 - d_r^2)}$$ bearing stress

$d = 3/8'' = 9.525\ mm$

$A_{dr} = 0.0809\ in^2 \Rightarrow d_r = 0.321\ in = 8.152$

$$\frac{\pi d_r^2}{4} = A_{dr}$$

$$d_r^2 = \frac{4}{\pi}(0.0809)$$

$d_r = 0.321\ in$

$$p = \frac{9.525 - 8}{10 - 8} = \frac{x - 1.25}{1.5 - 1.25}$$

$p = 1.44\ mm$

$h = 14\ mm$

$T = 6.764\ Nm = 2FR$

$\times 5$

$33.82\ Nm = 2FR$

$F_1 = \frac{33.82\ Nm}{(.0127\ m)2} = 2663\ N / 2 = 1331.5\ N$ from applied load

$F_2 = 60\ lb_f \times \frac{4.448\ N}{1\ lb_f} = 266.9\ N$

$F_{total} = 1598.4$

$\times 6.89\ MPa$

$$\sigma = \frac{-4(0.00144\ m)(1598.4\ N)}{\pi(.014\ m)(.009525\ m^2 - 0.008152^2)}$$

$\sigma = 8.625\ MPa$

$\sigma = 0.799\ ksi$

Proof strength for $\frac{1}{4} - \frac{3}{4}$ nominal diameter is 55 ksi

$\therefore$ screw is okay

A.4 MATERIALS VALIDATION

A.4.1 Materials and Methods

Validation was performed using the Interlaken Series 3300 test frame. Cast acrylic was chosen to validate the torsion system for its similarity in stiffness to bone and its machinability. Specimens were affixed at one end with a manual 5-C collet clamp and a steel cable regulated collet at the other end. By applying a uniaxial load, the cable wrapped collet produced a pure torque on the test material.

Angular displacement was measured using an optical system, capable of resolving 3μm displacements in three dimensional space. One millimeter square infrared (IR) reflective markers were adhered to the test material, and its relative positions monitored in three dimensional space with the MacReflex system (Sweden). Load and coordinates of the IR markers were collected synchronously using Biopac (Santa Barbara CA).

Four acrylic rods were turned down to 9.5mm cylinders with a gauge length of 25.4mm to displace approximately fifteen degrees at the maximum breaking strength of the cables. Cylinders were coated with black ink to reduce IR reflection, and two reflective markers were spaced 25.4mm apart, collinear with the primary axis and symmetric about the defect. A 56.5Nm loadcell was calibrated to 8.81Nm fullscale output, and the torsional load recorded at 12Hz synchronously with three dimensional coordinates of the two IR markers. Tests were conducted under linear displacement control, with a single ramp to 8mm cross-head displacement, at an average strain rate of 0.1%. Strain of the specimen between the markers was determined by the product of the relative angular displacement between the markers and the ratio between bulk radius to gauge length.

Theoretical shear modulus was calculated based on the linear relationship of shear modulus to elastic modulus and Poisson's Ratio. The elastic modulus was taken as 2757.9MPa and Poison's ration as 0.35 (Polycast Technology, Sterling NJ). The calculated theoretical shear modulus was 1021MPa. The experimental shear modulus was calculated using the slope from the linear region on the torque vs angular displacement curve multiplied by the ratio of the gauge length to the bulk polar moment of inertia. One acrylic cylinder was tested eleven times, and the coefficient of variation of the moduli was calculated to determine the precision of the system. Four acrylic cylinders were tested, and the average deviation from theoretical shear modulus was calculated to determine the accuracy of the system.

A.4.2 Results

A.4.2.1 Precision

Test	Experimental Shear Modulus (MPa)
1	924.1
2	893.2
3	896.7
4	935.7
5	946.4
6	942.7
7	922.3
8	896.1
9	888.7
10	886.8
11	907.5
Mean (MPa)	912.7
Stdev (MPa)	22.3
COV	2.44

A.4.2.2 Accuracy

Test Specimen	Shear Modulus (MPa)	% diff 1021MPa
Spec 1	1014.3	0.66
Spec 2	962.1	5.77
Spec 3	968.3	5.16
Spec 4	1062.7	4.08
	Mean (MPa)	3.92